

Expression of Interest for
A Novel Search for CP Violation in the
Neutrino Sector:



J. Alonso¹³, F.T. Avignone¹⁸, W.A. Barletta¹³,
R. Barlow⁵, H.T. Baumgartner¹³, A. Bernstein¹¹, E. Blucher⁴,
L. Bugel¹³, L. Calabretta⁹, L. Camilleri⁶, R. Carr⁶,
J.M. Conrad^{13,*}, S.A. Dazeley¹¹, Z. Djurcic², A. de Gouvêa¹⁷,
P.H. Fisher¹³, C.M. Ignarra¹³, B.J.P. Jones¹³, C.L. Jones¹³,
G. Karagiorgi¹³, T. Katori¹³, S.E. Kopp²⁰, R.C. Lanza¹³,
W.A. Loinaz¹, P. McIntyre¹⁹, G. McLaughlin¹⁶, G.B. Mills¹²,
J.A. Nolen², V. Papavassiliou¹⁵, M. Sanchez^{2,10}, K. Scholberg⁷,
W.G. Seligman⁶, M.H. Shaevitz^{6,*}, S. Shalgar¹⁷, T. Smidt¹³,
M.J. Syphers¹⁴, J. Spitz²², H.-K. Tanaka¹³, K. Terao¹³,
C. Tschalaer¹³, M. Vagins^{3,21}, R. Van de Water¹²,
M.O. Wascko⁸, R. Wendell⁷, L. Winslow¹³

October 1, 2018

- ¹Amherst College, Amherst, MA 01002, USA
- ²Argonne National Laboratory, Argonne, IL 60439, USA
- ³University of California, Irvine, CA 92697, USA
- ⁴University of Chicago, Chicago, IL 60637, USA
- ⁵The Cockcroft Institute for Accelerator Science &
the University of Manchester, Oxford Road, Manchester M13 9PL, UK
- ⁶Columbia University, New York, NY 10027, USA
- ⁷Duke University, Durham, NC 27708, USA
- ⁸Imperial College London. London, SW7 2AZ, UK
- ⁹Istituto Nazionale di Fisica Nucleare, Laboratori Nazionali del Sud,
I-95123, Italy
- ¹⁰Iowa State University, Ames, IA 50011, USA
- ¹¹Lawrence Livermore National Laboratory, Livermore, CA 94551, USA
- ¹²Los Alamos National Laboratory, Los Alamos, NM 87545, USA
- ¹³Massachusetts Institute of Technology, Cambridge, MA 02139, USA
- ¹⁴Michigan State University, East Lansing, MI 48824, USA
- ¹⁵New Mexico State University, Las Cruces, NM 88003, USA
- ¹⁶North Carolina State University, Raleigh, NC 27695, USA
- ¹⁷Northwestern University, Evanston, IL 60208, USA
- ¹⁸University of South Carolina, Columbia, SC 29208, USA
- ¹⁹Texas A&M University, College Station, TX 77843, USA
- ²⁰University of Texas, Austin, TX 78712, USA
- ²¹University of Tokyo, Kashiwa, 277-8583, Japan
- ²²Yale University, New Haven, CT 06520 USA

* Corresponding authors. For further information contact:
conrad@mit.edu, shaevitz@nevis.columbia.edu

Abstract

DAE δ ALUS, a **D**ecay-**A**t-rest **E**xperiment for δ_{CP} studies **A**t the **L**aboratory for **U**nderground **S**cience, provides a new approach to the search for CP violation in the neutrino sector. The design utilizes low-cost, high-power proton accelerators under development for commercial uses. These provide neutrino beams with energy up to 52 MeV from pion and muon decay-at-rest. The experiment searches for $\bar{\nu}_\mu \rightarrow \bar{\nu}_e$ at short baselines corresponding to the atmospheric Δm^2 region. The $\bar{\nu}_e$ will be detected, via inverse beta decay, in the 300 kton fiducial-volume Gd-doped water Cherenkov neutrino detector proposed for the Deep Underground Science and Engineering Laboratory (DUSEL).

DAE δ ALUS opens new opportunities for DUSEL. It provides a high-statistics, low-background alternative for CP violation searches which matches the capability of the conventional long-baseline neutrino experiment, LBNE. Because of the complementary designs, when DAE δ ALUS antineutrino data are combined with LBNE neutrino data, the sensitivity of the CP-violation search improves beyond any present proposals, including the proposal for Project X. Also, the availability of an on-site neutrino beam opens opportunities for additional physics, both for the presently planned DUSEL detectors and for new experiments at a future 300 ft campus.

Contents

1	Executive Summary	4
2	The Physics Opportunities of DAEδALUS	14
2.1	<i>CP</i> Violation and Neutrinos	14
2.1.1	Introducing <i>CP</i> Violation into the Light Neutrino Sector	15
2.1.2	<i>CP</i> Violation in Neutrino Oscillations	16
2.1.3	The Mass Hierarchy and Matter Effects	17
2.1.4	Oscillation Probability Calculations	19
2.2	DAE δ ALUS and <i>CP</i> Violation	19
2.2.1	Overview of the DAE δ ALUS Design	20
2.2.2	Events in the Detector	23
2.2.3	Systematic Errors Before Constraints	28
2.2.4	Oscillation Sensitivities	31
2.3	A Joint Analysis With the Fermilab Beam	35
2.3.1	LBNE Current Plans: ν (5 yr) + $\bar{\nu}$ (5 yr) Running . . .	35
2.3.2	DAE δ ALUS+LBNE (ν Only)	38
2.3.3	Comparing to Project X	39
2.4	Physics with a Near Accelerator	41
2.4.1	Coherent neutrino-nucleus scattering	41
2.4.2	Measurements useful for astrophysics	43
2.4.3	Neutrino magnetic moment	44
2.4.4	Measurement of Δs	45
3	Preliminary Design	48
3.1	Accelerator Design	48
3.1.1	Overview of Cyclotron Subsystems	49
3.1.2	Compact Cyclotrons	51
3.1.3	H $_2^+$ Cyclotrons	55

3.1.4	Stacked Cyclotrons	59
3.1.5	Other Types of Accelerators: Superconducting Linacs .	61
3.1.6	Neutrino Source Design	62
3.2	Detector Design	67
3.2.1	Gd Doping	67
3.2.2	Photocathode Coverage	72
3.3	A Three-Phase Implementation Plan	74
4	Impact On Other Analyses	78
4.1	Neutrino-electron Events as a Calibration Source	78
4.2	Impact On Other Large Detector Analyses	80
5	Conclusion	85

Chapter 1

Executive Summary

This Expression of Interest (EOI) describes DAE δ ALUS, a **Decay-At-rest Experiment for δ_{CP} studies At the Laboratory for Underground Science**. The primary physics goal of the experiment is to search for CP -violation in the neutrino sector using a novel design which provides high-statistics and low backgrounds [1]. DAE δ ALUS searches for CP violation in $\bar{\nu}_\mu \rightarrow \bar{\nu}_e$ oscillations at the atmospheric mass splitting by comparing absolute neutrino rates in a single detector that is exposed to neutrino beam sources at three distances. This method exploits the length-dependence of the CP -violating interference terms in the oscillation formula. The near-source measures the initial flux. The mid-source is at half of oscillation maximum. The far source is at oscillation maximum.

As discussed in Chapter 2, DAE δ ALUS has several advantages over conventional searches. The experiment can demonstrate that δ_{CP} , the CP -violating parameter in the three-neutrino mixing matrix, is not 0 or 180°, regardless of the mass hierarchy. Because this is a short-baseline experiment, it does not suffer from “apparent CP -violation” caused by matter effects. DAE δ ALUS matches the sensitivity of conventional long-baseline experiments (*e.g.*, LBNE [2]) to δ_{CP} and the mixing angle θ_{13} . Because the time-frame for constructing the accelerators is relatively short, construction need not begin before present experiments provide a measure of θ_{13} . Also because of its complementary design, DAE δ ALUS substantially improves the sensitivity of the search when the data are combined with the long-baseline results. Beyond oscillation physics, DAE δ ALUS enhances the physics opportunities at the Deep Underground Science and Engineering Laboratory by providing an on-site high-intensity neutrino source.

The neutrino beams will be produced via high-power proton cyclotron accelerators that are under development for Accelerator Driven Systems (ADS) for subcritical thorium-based reactors and for active interrogation for homeland security. DAE δ ALUS requires accelerators that can target protons between 650 and 1500 MeV at 1 MW or more. The beams will be delivered in alternating time periods (presently planned for 100 μ s duration), in order to allow events from each position to be uniquely identified. We propose to run the near, mid and far sites each with a 20% duty factor. Multiple accelerators may be required at each site, depending on the cyclotron design.

The preliminary design of the experiment is described in Chapter 3. Cyclotrons deliver protons into a beam stop creating a high intensity, isotropic decay-at-rest (DAR) neutrino beam arising from the stopped pion decay chain: $\pi^+ \rightarrow \nu_\mu \mu^+$ followed by $\mu^+ \rightarrow e^+ \bar{\nu}_\mu \nu_e$. The resulting $\bar{\nu}_\mu$ flux rises with energy to the 52.8 MeV endpoint (see Fig. 1.1), with a well-known energy dependence. Because most π^- capture before decay, the $\bar{\nu}_e$ fraction in the beam is $\sim 4 \times 10^{-4}$. For a DAR beam design, CP -violation in $\bar{\nu}_\mu \rightarrow \bar{\nu}_e$ oscillations can be addressed with neutrino sources located at 1.5 km (near), 8 km (mid) and 20 km (far). A schematic is shown in Fig 1.2. The advantage of a DAR beam is that the nature of the weak interaction alone drives the energy dependence. The flux from the three beams will be identical up to the relative normalization. This experiment will use the 300-kton 3-unit water Cherenkov detector at the 4850 ft level of DUSEL as the neutrino target. Water provides a target of free protons for the inverse beta decay (IBD) interaction: $\bar{\nu}_e + p \rightarrow n + e^+$. IBD interactions are identified via a coincidence signal: the Cherenkov ring produced by the positron followed by the capture of the neutron. Doping with gadolinium (Gd) is proposed in order to enhance the neutron capture signal [3, 4, 5, 6].

We propose a two phase search for CP -violation, where each phase represents five years of running. The purpose of Phase 1, which will have 1 MW, 2 MW and 3 MW accelerators at the near, mid and far locations is to explore the oscillation space with $\sim 3\sigma$. Once the region of interest is localized, additional neutrino sources can be added at appropriate locations for Phase 2 to give the best possible measurement. For simplicity, in this EOI, we will generally show results for the Phase 2 configuration of (1 MW, 2 MW, 7 MW), but it should be understood that this is just one example.

The analysis, described in Sec. 2.2, follows three steps. First, the absolute normalization of the flux from the near accelerator is measured using neutrino-electron scatters in the detector, for which the cross section is

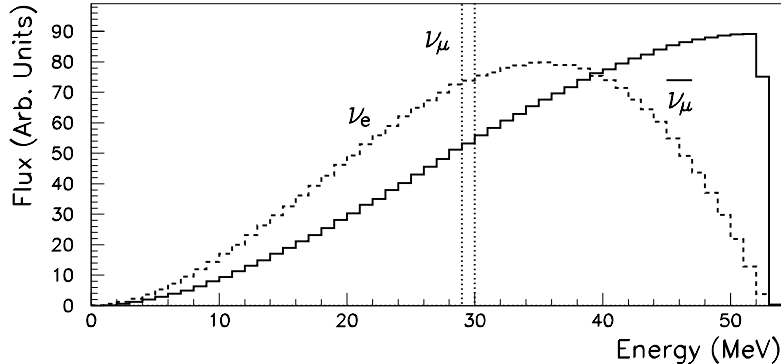


Figure 1.1: Energy distribution of neutrinos in a DAR beam

known to 1%. The relative flux normalization between the sources is then determined using the comparative rates of ν_e -oxygen interactions in the the detector. Once the normalizations of the accelerators are known, then the IBD data can be fit to extract the CP -violating parameter δ_{CP} . The χ^2 statistic of the fit accounts for systematic uncertainties through parameters that vary along with the oscillation parameters, but which are constrained by pull terms. The oscillation probability also depends on the mixing angle θ_{13} . Therefore, the resulting measurement must be described in a $\sin^2 2\theta_{13}$ - δ_{CP} plane.

Fig. 1.3 shows the 1 and 2σ contours for the combined DAE δ ALUS 2-phase running, where each point represents a hypothetical true value of $\sin^2 2\theta_{13}$ and δ_{CP} . This figure presents the results for the normal hierarchy of neutrino masses indicated along the left axis. DAE δ ALUS is a short-baseline experiment with an inherent ambiguity between the two hierarchies. For the inverted hierarchy, the corresponding value of δ_{CP} is shown on the right axis. The expectation for the two hierarchies can be presented in this way because DAE δ ALUS does not suffer from matter effects which introduce apparent CP -violation, unlike long-baseline experiments. This means that the value of δ_{CP} extracted by DAE δ ALUS will have an ambiguity until the hierarchy is known. However, DAE δ ALUS can determine if there is CP violation (i.e. $\delta_{CP} \neq 0$ or 180°) without this input.

As described in Sec. 2.3, DAE δ ALUS is designed to match the δ_{CP} and θ_{13} sensitivity of LBNE, the planned experiment which uses a conventional

long-baseline neutrino beam from FNAL to DUSEL. This experiment quotes capability based on 30×10^{20} protons on the FNAL target in neutrino and antineutrino mode, respectively [2]. We assume this will be delivered at a rate of 6×10^{20} protons on target per year [7], making for a 10 year run, the same length as the DAE δ ALUS run. While LBNE is designed to run for 5 years in neutrino mode and 5 years in antineutrino mode, its statistical strength is in neutrino mode. Statistics in antineutrino running are suppressed by a low production rate of π^- compared to π^+ and by a reduced cross section compared to that of neutrinos.

DAE δ ALUS and LBNE are complementary experiments:

- The DAE δ ALUS signal is entirely in antineutrino mode, while the statistical strength of LBNE is in neutrino running.
- DAE δ ALUS is a short-baseline experiment with no matter effects, while LBNE is a long-baseline experiment with matter effects.
- DAE δ ALUS events are at low energy and in a narrow energy-window from 20 to 52.8 MeV, while LBNE has a high energy, wide-band (300 MeV to about 10 GeV) signal.
- DAE δ ALUS has very low backgrounds, coming mainly from beam-off sources which can be well measured from beam-off running, while LBNE has a poorer signal-to-background ratio, but with very different systematics.

As a result of the complementarity, when the two experiments are combined, the sensitivity is substantially improved. Two scenarios which exploit the fact that LBNE's strength is in neutrino running are:

- DAE δ ALUS+LBNE ν —5 yr: A five-year run of both experiments, combining DAE δ ALUS Phase 1 with a 30×10^{20} POT ν -only LBNE data set.
- DAE δ ALUS+LBNE ν —10 yr: A ten-year run of both experiments, with the Phase 1 + 2 DAE δ ALUS sample combined with a 60×10^{20} POT ν -only LBNE data sample.

These can be compared to the standard 10-year running scenarios of DAE δ ALUS and LBNE. Fig. 1.4 shows the 3σ sensitivity for DAE δ ALUS+LBNE ν —5 yr

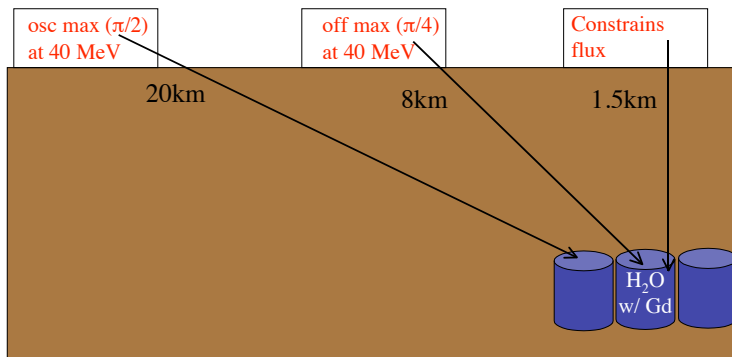


Figure 1.2: Schematic of the DAE δ ALUS Experiment. Three neutrino source locations are used in conjunction with the 300 kton water Cherenkov detector complex at the 4850 level of DUSEL.

and 10 yr scenarios. The combined samples allow exploration to very small values of $\sin^2 2\theta_{13}$. Fig. 1.5 provides the sensitivity, given the normal hierarchy for the 10 yr scenario. The expected errors are reduced by a factor of two compared to running either LBNE or DAE δ ALUS alone.

Fig. 1.6 shows the strength of the DAE δ ALUS+LBNE ν —10 yr scenario to LBNE running with Project X. This plot characterizes the capability of the experiments in terms of the fraction of δ_{CP} space which is 3σ from $\delta_{CP} = 0$ or 180° after a 10 year run. In the Project X scenario, LBNE would receive 2×10^{21} POT per year, with five years of running in neutrino mode and 5 years of running in antineutrino mode [8]. The Project X expectation is shown by the dashed line with \times s. The combined LBNE and DAE δ ALUS expectation, shown by the red line, is substantially better than the Project X scenario for measurement of δ_{CP} .¹ The combination also compares favorably

¹As this EOI reached its final draft, ref. [9] appeared on the arXiv, reporting the same conclusion, though for slightly different design parameters.

to second-generation super-beam facilities [10].

The near accelerator opens up opportunities for new physics measurements at DUSEL, as discussed in Sec. 2.4. The high intensity beam, with its well-measured flux normalization, will allow precise measurements of neutrino cross sections in the large water and liquid argon detectors up to 52 MeV. This is the region of interest for supernova studies. This beam will also allow calibration of the large detectors. Also, if the accelerator is placed in proximity to the proposed 300 ft level campus, a new program of small experiments could open up. Potential sites are discussed in Sec. 3.3.

We propose a Phase 0 run with only the near accelerator. This will allow us to learn to run the machines while at the same time allowing for a near accelerator physics program. This run would occur while the water Cherenkov detector is under construction. The installation of the other accelerators would be timed such that Phase 1 can begin when the water Cherenkov detector is complete.

In summary, the 3-phase run-plan, explained in Sec. 3.3, consists of:

1. **Learn:** Run the near accelerator to learn more about operations, as well as to make useful preliminary cross section measurements.
2. **Discover:** Run in the 1-2-3 MW configuration to discover the value of δ , while maintaining flexibility of design.
3. **Measure:** Run for the remainder of the experiment with the most optimal accelerator design.

This plan maximizes the physics capability of DAE δ ALUS. It also dovetails well with timing of expected results on the mixing angle θ_{13} from the reactor experiments and T2K [11]. Along with a clear intellectual logic to the plan, this three-phase design has the advantage of allowing for a smooth funding profile over a period of about a decade.

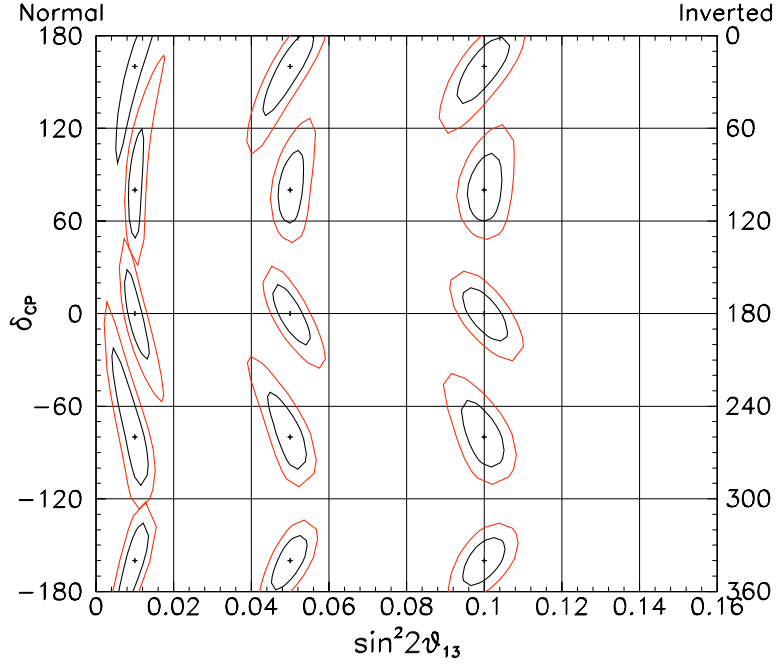


Figure 1.3: One (inner contour) and two (outer contour) σ sensitivities for DAE δ ALUS for Phase 1 and 2 combined (10 years of running). DAE δ ALUS is not sensitive to matter effects and, therefore, has a degeneracy between the two mass hierarchies. This can be represented by showing the δ_{CP} scale for normal hierarchy on the left and inverted on the right. DAE δ ALUS can determine if there is CP violation (i.e. $\delta_{CP} \neq 0$ or 180°) without this input. Details are provided in Sec. 2.2.

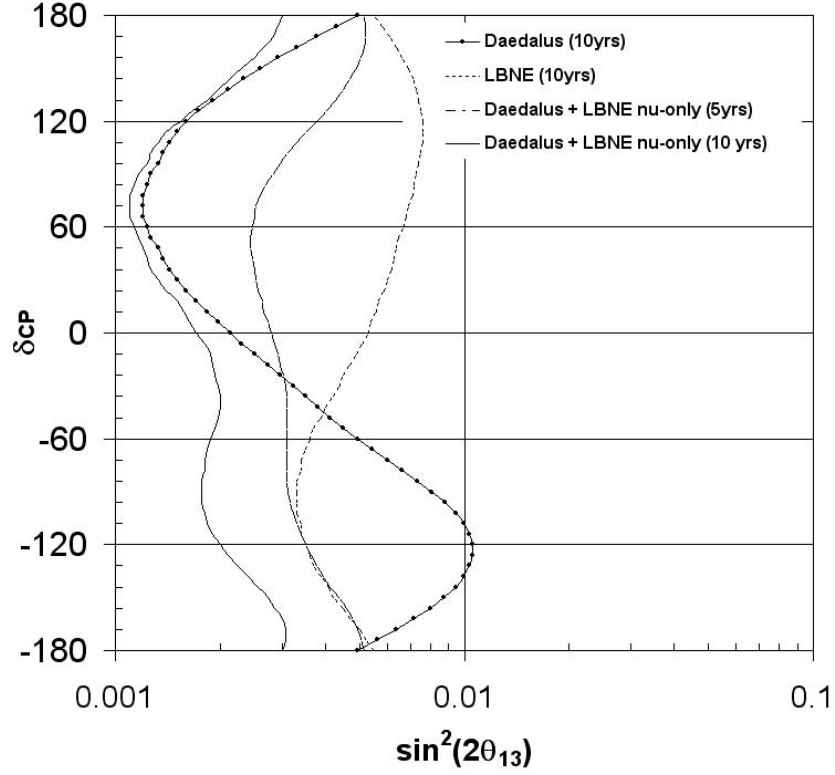


Figure 1.4: The 3σ confidence level sensitivity for determining a non-zero value for θ_{13} as a function of $\sin^2 2\theta_{13}$ and δ_{CP} . Solid-with-dots: DAE δ ALUS phase 1+2 result; Dashed: LBNE proposed running (30×10^{20} POT in ν mode and 30×10^{20} POT in $\bar{\nu}$ mode); Solid (Dot-dashed): the combined DAE δ ALUS plus LBNE ν -only result for 10 years (5 years). For the LBNE input, which is affected by matter effects, we assume normal hierarchy. Details are provided in Sec. 2.3.

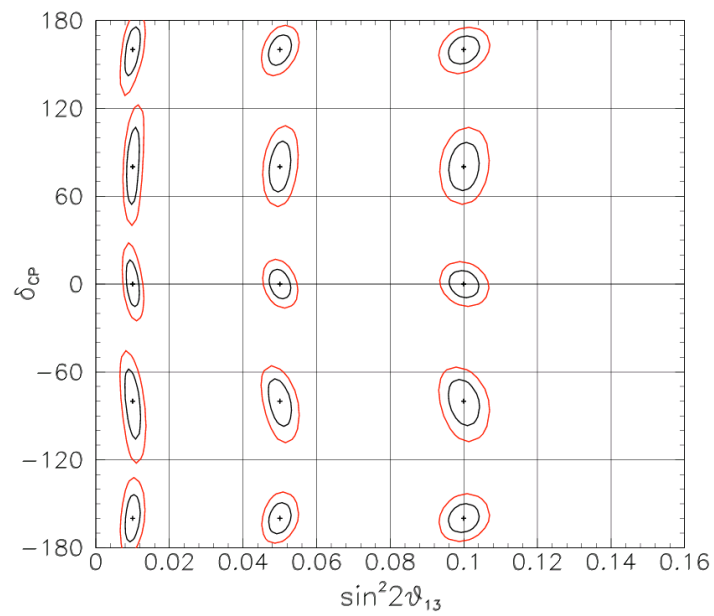


Figure 1.5: One (inner contour) and two (outer contour) σ sensitivities for the DAE δ ALUS+LBNE ν —10 yr scenario. Normal mass hierarchy is assumed for LBNE. Details are provided in Sec. 2.3.

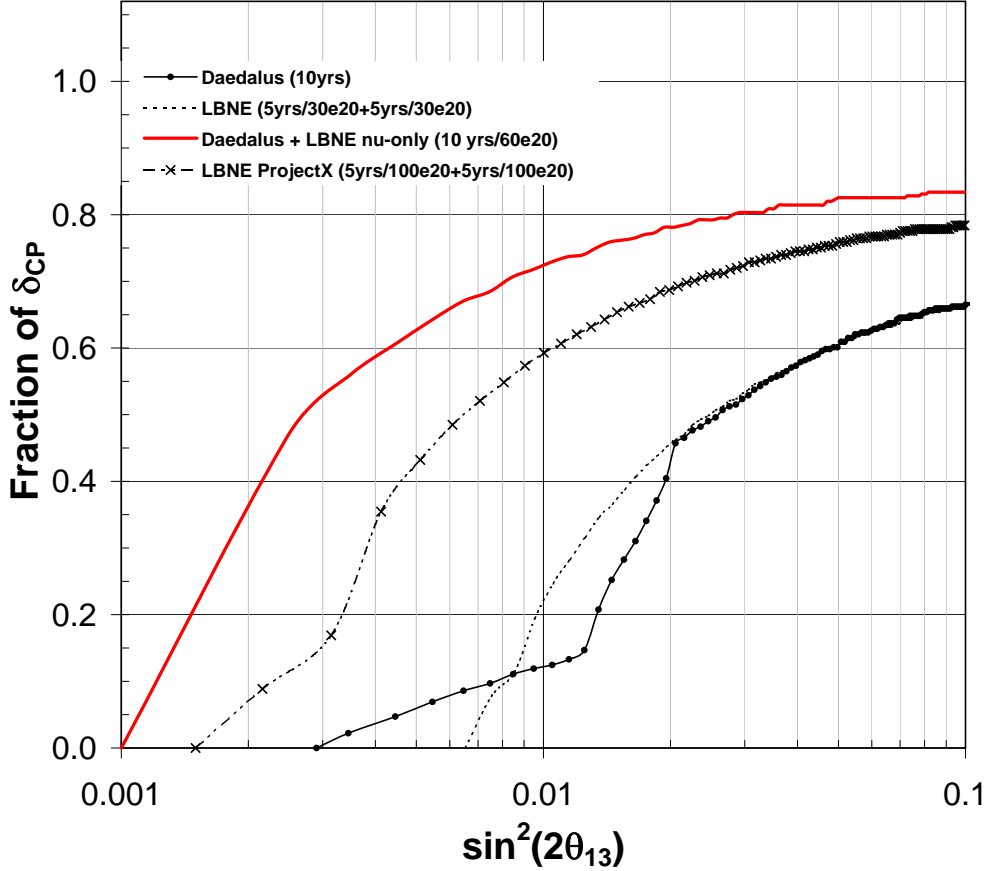


Figure 1.6: Fraction of δ_{CP} space over which a measurement can be differentiated from 0 or 180° at 3σ . Red solid: Combined sensitivity for the DAE δ ALUS+LBNE ν —10 yr scenario. Dashed with \times : Project X scenario for LBNE (5 years of running with 100×10^{20} protons on target in neutrino mode followed by 5 years of running 100×10^{20} protons on target in antineutrino mode). Expectations for standard running for DAE δ ALUS (solid line with dots) and LBNE dashed) are also shown. Normal mass hierarchy is assumed for LBNE. Details are provided in Sec. 2.3.

Chapter 2

The Physics Opportunities of DAE δ ALUS

2.1 CP Violation and Neutrinos

The search for CP violation in the light-neutrino sector is a priority of the particle-physics community [12, 13]. Interest has been sparked by models which invokes GUT-scale Majorana neutrino partners which can decay, producing a matter-antimatter asymmetry in the early universe through the mechanism of CP violation [14, 15, 16]. This process is called “leptogenesis.” Observation of CP violation in the light neutrino sector would be a strong hint that this theory is correct. At the same time, one can argue that the (dis)similarities of mixing in the lepton and quark sectors provide clues about the theory at the highest energy scale, and information on the relative level of CP violation in the sectors can push this even further (Refs. [17, 18] provide examples).

DAE δ ALUS, a short-baseline $\bar{\nu}_\mu \rightarrow \bar{\nu}_e$ experiment, approaches this high-priority search in a novel manner. In this section, we describe the theory of CP violation in the neutrino sector, with emphasis on those aspects specific to the DAE δ ALUS design.

2.1.1 Introducing CP Violation into the Light Neutrino Sector

One can introduce three physically-meaningful CP -violating phases into the model. For convenience, these are presented within the context of the product of two matrices: $U^{CP} = VK$. In this case, V is the traditional 3-neutrino oscillation mixing matrix with the addition of a CP violating phase, δ_{cp} :

$$V = \begin{pmatrix} c_{12}c_{13} & s_{12}c_{13} & s_{13}e^{-i\delta_{cp}} \\ -s_{12}c_{23} - c_{12}s_{23}s_{13}e^{i\delta_{cp}} & c_{12}c_{23} - s_{12}s_{23}s_{13}e^{i\delta_{cp}} & s_{23}c_{13} \\ s_{12}s_{23} - c_{12}c_{23}s_{13}e^{i\delta_{cp}} & -c_{12}s_{23} - s_{12}c_{23}s_{13}e^{i\delta_{cp}} & c_{23}c_{13} \end{pmatrix}. \quad (2.1)$$

This is analogous to the CKM matrix of the quark sector. The other term,

$$K = \text{diag}(1, e^{i\phi_1}, e^{i(\phi_2 + \delta_{cp})}) \quad (2.2)$$

has two further Majorana CP violating phases, ϕ_1 and ϕ_2 .

One would like to connect δ_{CP} , ϕ_1 and ϕ_2 to CP violation in heavy neutrinos at the GUT scale, since this might motivate leptogenesis. At present, there is no direct theoretical argument which does this. However, it is observed that in the Lagrangian, these all come from a matrix of Yukawa coupling constants. In principle, all of these phases can take on the full range of values, including exactly zero. However, it is difficult to motivate a theory in which some are nonzero and some are exactly zero. It is expected that these parameters will either all have non-zero values or all be precisely zero. If the latter is the case, then the difference between the lepton sector, with no CP violation, and quark sector, with clear CP violation, must be motivated. As a result, observation of CP violation in the light neutrino sector, through δ_{CP} or ϕ_1 and ϕ_2 , is regarded as the ‘‘smoking gun’’ for CP violation in the heavy sector. The ϕ phases arise as a direct consequence of the Majorana nature of neutrinos. Therefore, in principle, the ϕ phase is accessible in neutrinoless double beta decay. Even after neutrinoless double beta decay is observed, observation of the ϕ phases is expected to be extremely difficult because of uncertainties on the Matrix Element for neutrinoless double beta decay. Thus it seems likely that measurement of the ϕ phases is in the distant future. On the other hand, δ_{cp} , the ‘‘Dirac’’ CP -violating term in V may be accessible through oscillation experiments such as DAE δ ALUS.

2.1.2 CP Violation in Neutrino Oscillations

The parameter δ_{CP} is accessible through the muon-to-electron neutrino flavor oscillation probability. For oscillations in a vacuum, this is given by [19]:

$$\begin{aligned}
 P_{\mu \rightarrow e} = & \sin^2 \theta_{23} \sin^2 2\theta_{13} \sin^2 \Delta_{31} \\
 & \mp \sin \delta \sin 2\theta_{13} \sin 2\theta_{23} \sin 2\theta_{12} \sin^2 \Delta_{31} \sin \Delta_{21} \\
 & + \cos \delta \sin 2\theta_{13} \sin 2\theta_{23} \sin 2\theta_{12} \sin \Delta_{31} \cos \Delta_{31} \sin \Delta_{21} \\
 & + \cos^2 \theta_{23} \sin^2 2\theta_{12} \sin^2 \Delta_{21}
 \end{aligned} \tag{2.3}$$

where $\Delta_{ij} = \Delta m_{ij}^2 L / 4E_\nu$. In the second term, the $-(+)$ refers to neutrino (antineutrino) running. Traditionally, searches for CP violation through non-zero δ_{CP} have relied on comparing neutrino and antineutrino oscillation probabilities, exploiting this change of sign in order to isolate δ_{CP} . However, DAE δ ALUS will be a search only in antineutrino mode: $\bar{\nu}_\mu \rightarrow \bar{\nu}_e$, and so in our case, only the $+$ sign applies. Sensitivity to CP violation comes about through the interference between Δ_{12} and Δ_{13} transitions, which has a distinctive L dependence that we will exploit. Eq. 2.3 depends on many parameters. However, most are well-known. In Table 2.1, we provide a summary of the present level of knowledge of the parameters, as well as the improvement expected in the future, where ‘‘NIN’’ (No Improvement Needed) indicates that any future improvement does not impact the DAE δ ALUS analysis. Along with δ_{CP} , which is the focus of DAE δ ALUS, two other parameters, θ_{13} and the sign of Δm_{31}^2 , are unknown.

With respect to θ_{13} , global fits report a non-zero value at the $\sim 1\sigma$ level [20, 21]. This parameter drives the amplitude for the CP violating terms in Eq. 2.3 and therefore sets the level of technical difficulty for observing CP violation. There is a clear road-map toward discovery and measurement of θ_{13} within the present neutrino program [11] which dovetails well in time with the DAE δ ALUS search. DAE δ ALUS data will provide some constraint on $\sin^2 \theta_{13}$; however, the external data remain important to the analysis. Because there is a dependence on both δ_{CP} and $\sin^2 2\theta_{13}$, the DAE δ ALUS sensitivity must be expressed in a δ_{CP} - $\sin^2 2\theta_{13}$ plane, as shown in Fig. 1.3.

The unknown sign of Δm_{31}^2 , referred to as ‘‘the mass hierarchy,’’ will lead to an inherent degeneracy in the DAE δ ALUS analysis. From Eq. 2.3, one can see that for the DAE δ ALUS $\bar{\nu}_\mu \rightarrow \bar{\nu}_e$ search, the probabilities for the combination $(\delta_{CP}, \text{sign}(\Delta m_{31}^2) = +1)$ and $(180 - \delta_{CP}, \text{sign}(\Delta m_{31}^2) = -1)$ are equal. In the text below, we will refer to $\text{sign}(\Delta m_{31}^2) = +1$ as the ‘‘normal

Parameter	Present:			Assumed Value	Future:	
	Value	Uncert. (\pm)	Ref.		Uncert. (\pm)	Ref.
$\Delta m_{21}^2 \times 10^{-5} \text{eV}^2$	7.65	0.23	[20]	7.65	NIN	NIN
$\Delta m_{31}^2 \times 10^{-3} \text{eV}^2$	2.40	0.12	[20]	2.40	0.02	[22]
$\sin^2(2\theta_{12})$	0.846	0.033	[20]	0.846	NIN	NIN
$\sin^2(2\theta_{23})$	1.00	0.02	[20]	1.00	0.005	[23]
$\sin^2(2\theta_{13})$	0.06	0.04	[21]	0.05	0.005	[24]

Table 2.1: Left: Present values and uncertainties for oscillation parameters, reported in the listed references. Right: Future expectations used in this study, based on assumptions from the associated references. *NIN* means “No Improvement Needed” for the DAE δ ALUS analysis – the present values are sufficiently precise.

hierarchy” and $\text{sign}(\Delta m_{31}^2) = -1$ as the “inverted hierarchy.” Given that the degeneracy is perfect, we can express the DAE δ ALUS sensitivity for normal and inverted hierarchy on the same plot. In Fig. 1.3, the left vertical axis assumes the normal hierarchy and the right vertical axis assumes the inverted hierarchy.

2.1.3 The Mass Hierarchy and Matter Effects

External information will be required in order to break the mass hierarchy degeneracy in DAE δ ALUS. There are two sources of this information. First, the next generation neutrinoless double beta decay experiments, when combined with neutrino mass measurements from cosmology or direct searches, can, in principle, demonstrate the inverted mass hierarchy, if neutrinos are Majorana [25]. On the other hand, if no signal is seen, one does not know whether the hierarchy is normal or if neutrinos are not Majorana. A second approach is to use “matter effects” in muon-to-electron-neutrino, long-baseline, oscillation searches. These occur because neutrino and antineutrino beams will have a different forward-scattering amplitude as the beam propagates through the earth. The result is an “effective CP violation” — a difference in the rate of neutrino versus antineutrino oscillations which arises from some effect other than CP violation in the lepton- W coupling. These arise regardless of whether neutrinos are Majorana in nature or not.

Matter effects result in a modification of Eq. 2.3:

$$\begin{aligned}
P_{\text{mat}} &= \\
&\sin^2 \theta_{23} \sin^2 2\theta_{13} \frac{\sin^2 (\Delta_{31} \mp aL)}{(\Delta_{31} \mp aL)^2} \Delta_{31}^2 \\
&\mp \sin \delta \sin 2\theta_{13} \sin 2\theta_{23} \sin 2\theta_{12} \sin \Delta_{31} \frac{\sin (\Delta_{31} \mp aL)}{(\Delta_{31} \mp aL)} \Delta_{31} \frac{\sin (aL)}{(aL)} \Delta_{21} \\
&+ \cos \delta \sin 2\theta_{13} \sin 2\theta_{23} \sin 2\theta_{12} \cos \Delta_{31} \frac{\sin (\Delta_{31} \mp aL)}{(\Delta_{31} \mp aL)} \Delta_{31} \frac{\sin (aL)}{(aL)} \Delta_{21} \\
&+ \cos^2 \theta_{23} \sin^2 2\theta_{12} \frac{\sin^2 (aL)}{(aL)^2} \Delta_{21}^2. \tag{2.4}
\end{aligned}$$

In this equation, $a = \frac{G_F N_e}{\sqrt{2}}$ and \mp refers to neutrinos (antineutrinos). The same terms which are modified by the matter effects also will depend upon $\text{sign}(\Delta m_{31}^2)$. Because of this, the matter effects provide sensitivity to the mass hierarchy. Matter effects only appear when L is large, because $a \approx (3500 \text{ km})^{-1}$, for $\rho Y_e = 3.0 \text{ g/cm}^3$, is small. Short-baseline experiments, such as DAE δ ALUS, suffer negligible matter effects, and this is even true of moderate baseline experiments such as T2K [24], which is at 295 km. However the new generation of proposed long baseline beams, starting with Nu ν A [26], at 730 km, and moving on to longer baselines in Japan [27] and the US [2], at > 1000 km, will be sensitive to matter effects.

Matter effects are interesting in their own right. However, if one seeks to study CP violation in the lepton- W coupling in the same experiment, they have to be measured and removed. This is challenging if $\sin^2 2\theta_{13}$ is small, as one can see from Eq. 2.4. Also, if the hierarchy is inverted, the neutrino oscillation probability is suppressed, substantially reducing the statistics for neutrino oscillations. The result is that the mass hierarchy may be difficult to determine using this method, unless $\sin^2 2\theta_{13}$ is large.

In summary, DAE δ ALUS will have negligible matter effects. As a result, our experiment has sensitivity to CP -violation without complications of an extra source of effective CP violation. This offers a more straight-forward method of discovering and measuring δ_{CP} . However, it means that a degeneracy with the mass hierarchy will remain until $\text{sign}(\Delta m_{31}^2)$ is measured in some other experiment.

2.1.4 Oscillation Probability Calculations

The code used for calculating the oscillation probabilities presented in this EOI was written by Stephen Parke of Fermi National Accelerator Laboratory. The calculation uses the equations provided in Ref. [19]. The full formula, including matter effects, is used in all probability calculations presented in this EOI.

The collaboration has also implemented the DAE δ ALUS neutrino fluxes in the GLoBES neutrino oscillation simulation program [28]. We have verified that the probability calculations from the Parke code match the calculations from GLoBES. In the near future, we plan to contact the GLoBES authors in order to include these fluxes in the open-source GLoBES package.

2.2 DAE δ ALUS and CP Violation

The primary goal of DAE δ ALUS is to search for CP violation in a complementary manner to the present plans [24, 2]. The present suite of experiments is based on long-baseline “conventional” neutrino beams. These beams are produced by impinging high-energy protons on a target, resulting in pions and kaons which are sign-selected and focused by a magnet in the direction of a neutrino detector located ~ 1000 km away. CP violation is explored by comparing the rates of $\nu_\mu \rightarrow \nu_e$ to $\bar{\nu}_\mu \rightarrow \bar{\nu}_e$. These experiments are hampered by a lack of antineutrino statistics and by poor signal-to-background ratio. These experiments have the added complication of matter effects.

Given the high priority placed on a convincing measurement of δ_{CP} , should it be nonzero, we were motivated to develop a design which addresses these issues. We propose to use pion decay-at-rest beams, which produce muon antineutrinos peaked at 50 MeV, at three locations at short baseline to a large detector. This design will provide a high-statistics data sample which explores CP violation through the L dependence of the interference terms of Eq. 2.3. The measurement is novel in that it is done with antineutrinos exclusively, while all existing proposals rely most heavily on neutrino data. The antineutrino flux uncertainties are different from the flux uncertainties of conventional beams and are well-controlled. Because of the low beam energy, the interaction systematics are also different from those of the present program. Varying L , while employing a single detector, is novel for an appearance experiment (though it has been successfully employed at

KamLAND [29] and Super-K [30] for disappearance) and reduces systematics. A two-phase program which allows an optimized measurement strategy is powerful and potentially cost-saving.

This chapter very briefly describes the design of the experiment. This is followed by an extended discussion of event types, backgrounds and systematics in order to justify the sensitivity which is presented in Fig. 1.3. More information on design specifics and issues is then provided in the following chapters.

2.2.1 Overview of the DAE δ ALUS Design

DAE δ ALUS searches for $\bar{\nu}_\mu \rightarrow \bar{\nu}_e$ oscillations using neutrinos from three stopped-pion, decay-at-rest (DAR) beams, which interact in the 300 kton, Gd-doped water Cherenkov detector at DUSEL. This results in low systematics for the beam and detector. The shape of the DAR flux with energy is known to high precision and is common among the various distances, thus shape comparisons will have small uncertainties. The neutrino flux from the three distances is accurately determined from the direct measurement of the π^+ production rate using neutrino-electron scattering events from the near accelerator. The interaction and detector systematic errors are low since all events are detected in a single detector. The neutrino-electron cross section for normalization and inverse-beta-decay cross section for the signal are well-known. The fiducial volume error on the IBD events is also small due to the extreme volume-to-surface-area ratio of the ultra-large detector.

The beams are to be produced by proton accelerators with kinetic energy in the 650 MeV to 1.5 GeV range. In this range, the Δ resonance dominates π^+ production and little energy is lost to the production of other particles, such as neutrons or π^- s. As a result, in this energy range, for a given total power on target, the number of neutrino events produced by a DAR beam is flat as a function of proton energy; see Fig. 2.1.

Our proposal is to use low-cost cyclotrons, which are under development for commercial use, to provide the proton beams. Development of high intensity cyclotrons which are ~ 1 GeV is being driven by interest in accelerator driven systems (ADS) for thorium reactors and active interrogation for homeland security. The work builds upon the recent development of cyclotrons for medical uses. These cyclotrons are generally of two types: ~ 30 MeV and high power for PET isotope production and ~ 250 MeV and low power for cancer therapy. The evolution from medical machines to high powered, ~ 1

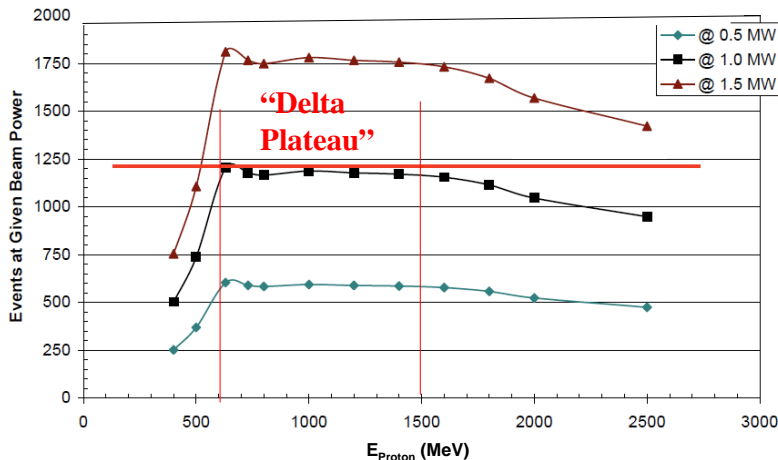


Figure 2.1: $\bar{\nu}_\mu$ production (arbitrary units) as a function of proton energy for 0.5, 1.0 and 1.5 MW on target

GeV machines does require further development, and there are none on the market today. However, we have found three groups interested in developing and commercializing cyclotrons which will satisfy our needs over the next few years. Machine options are discussed in Chapter 3.1.

Neutrinos are produced through the decay chain

$$\pi^+ \rightarrow \nu_\mu \mu^+ \quad (2.5)$$

$$\leftrightarrow \bar{\nu}_\mu e^+ \nu_e, \quad (2.6)$$

with a flux shown in Fig. 1.1. The shape of this energy distribution is defined by the weak interaction, but the overall normalization may vary between beam stops. We describe how we normalize the accelerator sources using events in the detector in the discussion below. This beam is isotropic, so the orientation of the accelerator with respect to the detector does not affect the fluxes of these three flavors. On the other hand, $\bar{\nu}_e$ is produced at the $\sim 10^{-4}$ level, as discussed below, from the chain of π^- which decay in flight. This background can be significantly reduced by pointing the primary beam at 120° or more with respect to the detector [31]. The $\bar{\nu}_e/\nu_e$ ratio also can be suppressed by designing the beamstops with a low- A target surrounded by a

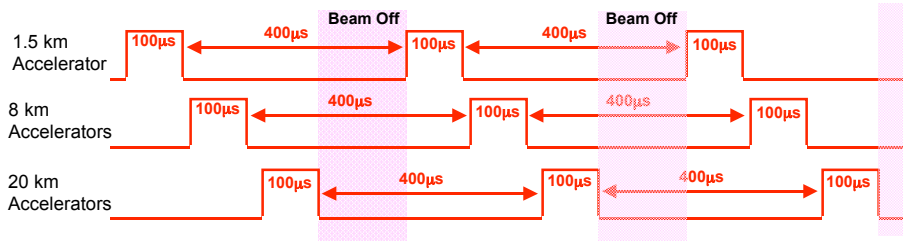


Figure 2.2: The source accelerator for events is identified through timing. We propose to run each accelerator with a 20% DF. Beam-off time allows measurement of non-beam-backgrounds. The timing structure presented here is illustrative, and longer intervals are not an issue for the analysis.

high- A absorber [32, 33]. The oscillated neutrinos are detected through the inverse-beta-decay (IBD) interaction, $\bar{\nu}_e + p \rightarrow e^+ + n$. This interaction has a high cross section at ~ 50 MeV, but requires a detector with a high fraction of free protons. The large water Cherenkov detector at DUSEL, which is proposed to be 300 ktons, is ideal for this. Should DUSEL choose to install a large liquid-scintillator module, this could also be used, though we do not present details here. The large liquid-argon detectors cannot be used for this analysis because there are no free proton targets.

In order to differentiate the signal IBD interactions from ν_e interactions, Gd-doping of the detector is required [3]. Fortunately, interest in studying supernova relic neutrinos and in using the large detector for non-proliferation studies has pushed forward techniques for Gd-doping water [4, 5, 6]. Gd-doping is within the scope of the S4 development. We discuss the issue of Gd-doping further in Chapter 3.2.

The accelerators will be positioned at 1.5, 8, and 20 km from the large water Cherenkov detector. The 1.5-km, “near accelerator” position is 4850 feet from the detector — that is, the accelerator remains above ground. The complexity of running the accelerators is sufficiently high to make above-ground running desirable. This accelerator will be on the DUSEL site. The 1.5-km accelerator allows measurement of the beam-on backgrounds and the normalization. The 8-km site is at an oscillation wavelength of about $\pi/4$ at 50 MeV and the 20-km site is at oscillation max for this energy. These two

accelerators are referred to as the “signal accelerators,” below. The location for these accelerators are off the DUSEL site and will need to be negotiated. We have in mind other mining sites which are no longer in use, but which have access roads and power.

We plan to run each site for 20% of the time; see Fig. 2.2. This allows us to use the time-stamp to identify which events come from each accelerator site. IBD events do not have a strong angular dependence [34], and so event-pointing cannot be used to connect events to a given accelerator. This also allows time for beam-off running, in order to measure non-beam-related backgrounds. Our initial proposal is to run each accelerator for 100 μ s, with 400 μ s beam-off. However, other timing patterns can be considered, up to intervals of minutes and even hours. During the interval that a given accelerator is on, it is run continuously (“*cw*”). We propose a phased running plan over 10 years. In Phase 1, we begin with 1 MW, 2 MW and 3 MW at the respective 1.5-km, 8-km, and 20-km sites. The purpose of this run is to discover *CP*-violation at the 3σ level, which is a 5-year run. At that point, more accelerators can be added in the proportion which is most advantageous to measuring the signal. Fig 1.3 is for a 2-phase run where the second 5-year period has 1, 2 and 7 MW at the three respective sites.

2.2.2 Events in the Detector

2.2.2.1 Neutrino Interactions of Interest to the Analysis

There are three important event types in this analysis: neutrino-electron scatters, ν_e -oxygen scatters, and IBD Events. The event rates for the 10 year run are shown in Table 2.2. The energy ranges for the analysis are listed below. The lower energy bound for the event samples is chosen to maintain a region of high signal-to-background. The upper bound is just above the 52.8 MeV endpoint of the neutrino spectra.

Neutrino-electron scatters During the 10-year run, 21.5k events will be collected from the near accelerator. Because the cross section for these events is known to better than 1% [35], these events can be used to obtain a precise measure of the near-accelerator flux normalization. The neutrino-electron analysis uses events in the visible energy range of 10 to 55 MeV. Neutrino-electron scatters can be separated from ν_e -oxygen scatters by angular cuts

Event Type	1.5 km	8 km	20 km
IBD Oscillation Events ($E_{vis} > 20$ MeV)			
$\delta_{CP} = 0^0$, Normal Hierarchy	763	1270	1215
” , Inverted Hierarchy	452	820	1179
$\delta_{CP} = 90^0$, Normal Hierarchy	628	1220	1625
” , Inverted Hierarchy	628	1220	1642
$\delta_{CP} = 180^0$, Normal Hierarchy	452	818	1169
” , Inverted Hierarchy	764	1272	1225
$\delta_{CP} = 270^0$, Normal Hierarchy	588	870	756
” , Inverted Hierarchy	588	870	766
IBD from Intrinsic $\bar{\nu}_e$ ($E_{vis} > 20$ MeV)	600	42	17
IBD Non-Beam ($E_{vis} > 20$ MeV)			
atmospheric $\nu_\mu p$ “invisible muons”	270	270	270
atmospheric IBD	55	55	55
diffuse SN neutrinos	23	23	23
ν -e Elastic ($E_{vis} > 10$ MeV)	21570	1516	605
ν_e -oxygen ($E_{vis} > 20$ MeV)	101218	7116	2840

Table 2.2: Event samples for the combined two-phase run for $\sin^2 2\theta_{13} = 0.05$ and parameters from Table 2.1 (future).

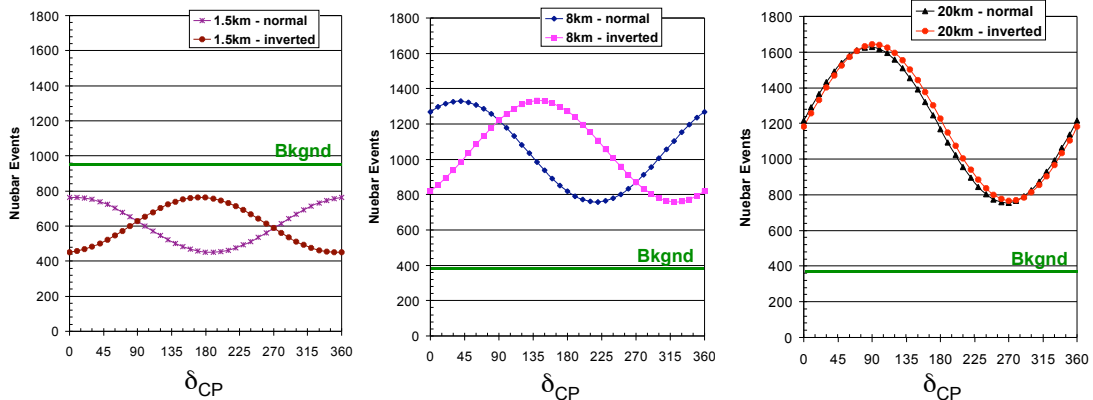


Figure 2.3: The oscillation event distribution as a function of δ_{CP} from each accelerator for the 10 year run, assuming $\sin^2 2\theta_{13} = 0.05$. The green line indicates the level of background for each data set.

[36, 37]. We estimate the reconstruction efficiency of these events as $\epsilon_{\text{recon}} = 75\%$ based on Ref. [36]

ν_e -oxygen scatters During the 10-year run a large sample of these events are collected from all three accelerators. The cross section is suppressed compared to the IBD cross section, because the target nucleons are bound [38, 39]. The cross section is not well-known, and we use a parameterization from Ref. [38], which gives the smaller predicted data set. (We note that an outcome of DAE δ ALUS will be a precise measurement of this cross section from the near accelerator data set, as discussed in Sec. 2.4). The sample from the 20-km accelerator is on the order of 2800 events, implying a 2% statistical error, for visible energy between 20 and 55 MeV. Comparing the rates between the three accelerators, adjusting for the $1/r^2$ dependence of the flux, allows determination of the normalization across the sites. We estimate the reconstruction efficiency of these events as $\epsilon_{\text{recon}} = 75\%$.

IBD Events These are the signal events for $\bar{\nu}_\mu \rightarrow \bar{\nu}_e$ oscillations. The number of events, therefore, depends upon the oscillation parameters. Fig. 2.3

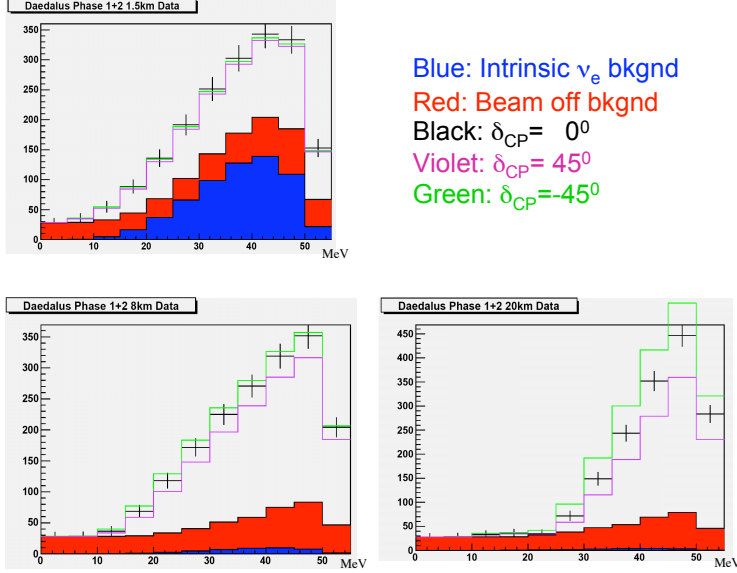


Figure 2.4: The event energy distributions for signal and background at $\sin^2 2\theta_{13} = 0.04$. Black, green and violet histograms show signals for $\delta_{cp} = 0$, 45° and -45° . The blue histogram shows the intrinsic $\bar{\nu}_e$ beam-on background. The red histogram shows the beam-off backgrounds. Top row: the near accelerator events. Bottom row: events in the signal accelerators

shows how the event rate from the three accelerators varies for the 10 year run, as a function of δ_{CP} , assuming $\sin^2 2\theta_{13} = 0.05$. One can see that the design leads to roughly equal signal samples from the 8-km and 20-km accelerator. One can also see that the 1.5-km accelerator will have signal events, and this must be included in the fits. Events in the energy range of 20 to 55 MeV will be used in the analysis, and the distribution of events is strongly peaked at about 50 MeV; see Fig. 2.4. As a result, DAE δ ALUS may be thought of as a narrow-band beam experiment. In this energy range, three types of interactions must be considered. First is the IBD signal, with an estimated reconstruction efficiency of $\epsilon_{recon} = 67\%$, based on studies for Super-K [4].

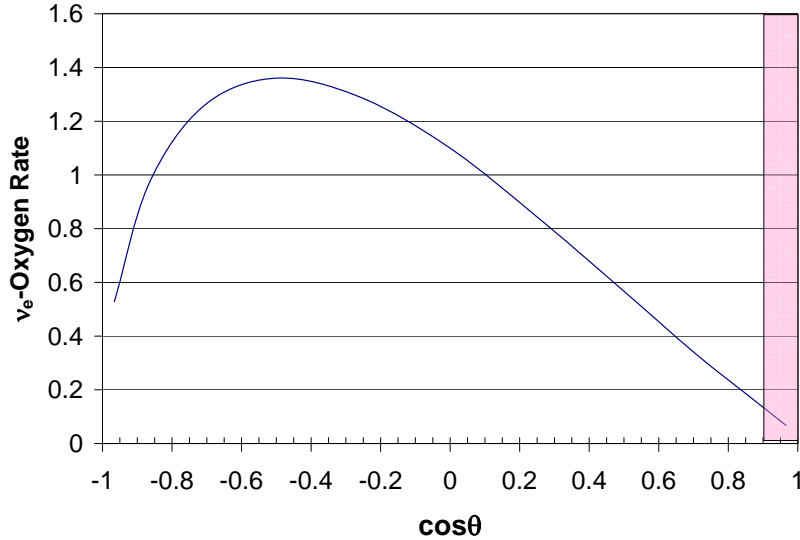


Figure 2.5: Rate of ν_e -oxygen events as a function of scattered electron angle. The shaded region, with $\cos\theta > 0.90$, is the region which the neutrino-electron scatters will populate.

2.2.2.2 Background Events

The total background from each accelerator is indicated by the green lines on Fig. 2.3. The energy distribution of the backgrounds compared to the expected events for $\sin^2 2\theta_{13} = 0.04$ and three values of δ_{CP} are shown in Fig. 2.4. One can see that the near accelerator (left in Fig. 2.3 and top in Fig. 2.4) provides a high-statistics sample for the beam-on background measurement. Because the isotropic beam produces backgrounds that fall as $1/r^2$, the signal accelerators have very little beam-on background. In the signal accelerators, the beam-off background dominates.

The beam-on backgrounds are dominated almost entirely by intrinsic $\bar{\nu}_e$ events in the beam. In principle, correlated beam-on backgrounds may be produced by ν_e charged current (CC) scatters in which a neutron is emitted. This is of special concern for interactions with ^{17}O and ^{18}O , which have natural abundances of 0.04% and 0.20%, respectively. We find that the rate of neutron production is negligible from excited ^{16}F [40], ^{17}F [41], and ^{18}F [42]. However, excited ^{18}F will decay to nitrogen plus an α . Data from the

(α , n) interaction on oxygen indicate about 1×10^{-8} neutrinos per 3 MeV α [43]. Hence, we expect this background to be negligible. The accidental backgrounds arise from the ν_e in the beam that are followed by a neutron-like event. This background is estimated to be very small using the measurements from the Super-K Gd-doping study [4]. As a result, in Figs. 2.3 and 2.4 we only show the intrinsic ν_e background, as the blue histogram. However, in the final data analysis all background sources are included.

Beam-off backgrounds arise from atmospheric $\nu_\mu p$ scatters with muons below Cherenkov threshold that stop and decay (“invisible muons”), atmospheric $\bar{\nu}_e$ IBD events, and supernova relic neutrinos. These are all examples of correlated backgrounds. The rates of these correlated backgrounds are scaled from analyses for the GADZOOKS experiment [3]. As, this study was done for the latitude of Super-K, not for DUSEL, in the future the level of this background will need to be adjusted; however, this study is sufficient for illustrative purpose in this EOI. The interaction rates of the beam-off backgrounds will be well-measured during the 40% beam-off running fraction. Thus the dominant beam-off error is the statistical error from the bin-by-bin background subtraction.

2.2.3 Systematic Errors Before Constraints

In the analysis, initial systematic uncertainties are assigned to quantities, which are then further constrained by fits to the DAE δ ALUS data set. Tab 2.3 provides the inputs for the systematics in the fit. The resulting final systematic error, after constraints, is at the level of 2%.

Because the flux chain begins with π^+ production, this systematic error is common to all types of events in the normalization and signal samples. This uncertainty is not well known, but becomes highly constrained when we use the neutrino-electron sample to set the overall normalization. Thus the analysis is insensitive to the level we assume as an input systematic uncertainty, which we take to be 10% here.

For the neutrino-electron sample, the largest systematic uncertainty comes from knowledge of the energy scale at $E_{\text{vis}} = 10$ MeV, the position of the cut in this analysis. This estimate comes from Super-K [44] and leads to a 1% error on the DAR flux normalization. However, we think that this is an overestimate. As we discuss in Sec. 4.1, the energy dependence of the neutrino-electron sample is very well predicted. Demanding that the ratio

Systematics on the Normalization	
<i>On all events</i>	<i>Fractional Uncertainty</i>
π^+ production	0.100
<i>Neutrino-electron scattering events</i>	<i>Fractional Uncertainty</i>
2.1% energy scale uncertainty	0.010
Cross section error from NuTeV $\sin^2 \theta_W$	0.005
Background subtraction systematics	0.000
<i>ν_e-oxygen scattering</i>	<i>Fractional Uncertainty</i>
Cross section	0.100
Systematics on the Signal	
<i>Oscillation IBD events</i>	<i>Fractional Uncertainty</i>
Efficiency of neutron detection	0.005
Fiducial volume	0.000
Systematics on the Backgrounds	
<i>Intrinsic $\bar{\nu}_e$ IBD Events</i>	<i>Fractional Uncertainty</i>
π^- production	0.100
π^- decay-in-flight	0.100
μ^- decay-in-flight	0.050
<i>Beam-off subtraction</i>	<i>Fractional Uncertainty</i>
Statistical error for Phase 1 period	0.054
Statistical error for Phase 2 period	0.038

Table 2.3: Systematic errors which are inputs to the fits. The systematics are then further constrained by the event samples in the fit.

$\sin^2 2\theta_{13}/\delta_{CP}$	-180	-90	0	90	135
0.01	52.5	47.2	29.0	38.8	48.5
0.05	21.6	21.9	19.5	25.6	30.4
0.09	18.3	19.9	17.6	23.8	26.3
0.01	51.3	45.5	26.9	36.7	46.9
0.05	19.9	21.2	18.2	24.2	29.6
0.09	16.8	19.2	16.5	22.6	25.3

Table 2.4: The 1σ measurement uncertainty on δ_{CP} for various values of $\sin^2 \theta_{13}$ for the combined two-phase data. Top: Systematic and statistical errors. Bottom: Statistical error only.

of measured to predicted energy distribution be flat should allow for energy calibration to better than 1%. The next largest error is due to the error on the cross section normalization from our knowledge of $\sin^2 \theta_W$. The LEP and SLAC results provide a precision measurement of $\sin^2 \theta_W$ which is in 3σ disagreement with the NuTeV deep inelastic neutrino scattering results (for discussion see Ref. [45]). Taking an agnostic viewpoint, we assign a systematic error which covers this disagreement, leading to the cross section error in Table 2.3.

The analysis relies on obtaining a pure sample of neutrino-electron scatters. The ν_e events on oxygen and IBD events with a missing neutron represent potential sources of background. However, these can be separated from the neutrino-electron sample since the angular distribution of neutrino-electron events is very forward-peaked, while ν_e -oxygen scatters have a broad distribution [37], as shown in Fig. 2.5. Only 0.8% of the ν_e -oxygen events have $\cos \theta > 0.90$ (*i.e.*, $\theta < 25^\circ$), as shown by the shaded region, giving a less than 4% background to the IBD sample. These backgrounds can be measured in the $\cos \theta < 0.90$ region and extrapolated into the neutrino-electron signal region, allowing them to be subtracted with negligible error, as we explicitly list in Table 2.3.

The largest input uncertainty on the IBD signal events arises from neutron-tagging and is taken to be 0.005. We also considered a fiducial volume error. Because the volume-to-surface area is so high in these large detectors, we find this error to be negligible.

The largest systematics associated with the intrinsic $\bar{\nu}_e$ background are related to the π^- production and decay chain. However the final analysis is

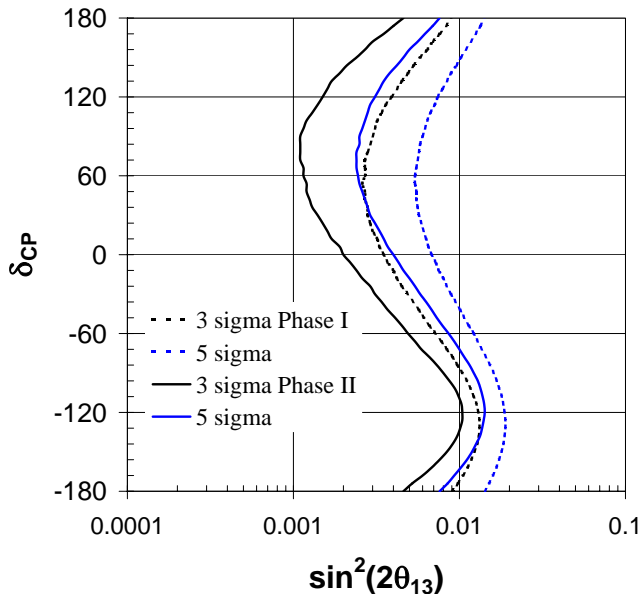


Figure 2.6: Phase-1 and Combined-phase sensitivity to $\theta_{13} \neq 0$ at 3σ and 5σ .

insensitive to these effects for two reasons. First, the near accelerator provides a high precision *in-situ* measure of the background. Second, because of the $1/r^2$ dependence of this flux in the signal accelerators, the rate is small (see blue histograms in Fig. 2.4, bottom).

The beam-off rates are measured rather than predicted. Therefore the systematic error associated with this source comes from the statistical error on the background subtraction.

2.2.4 Oscillation Sensitivities

Sensitivity estimates were made using a method similar to that described in Ref. [24]. Data are generated according to the experimental expectations with assumed underlying parameters. For a given set of new parameters, a standard χ^2 value is found by comparing the prediction with these parameters to the originally generated data. The difference between this χ^2 value and the one calculated with the original parameters is the χ^2 value.

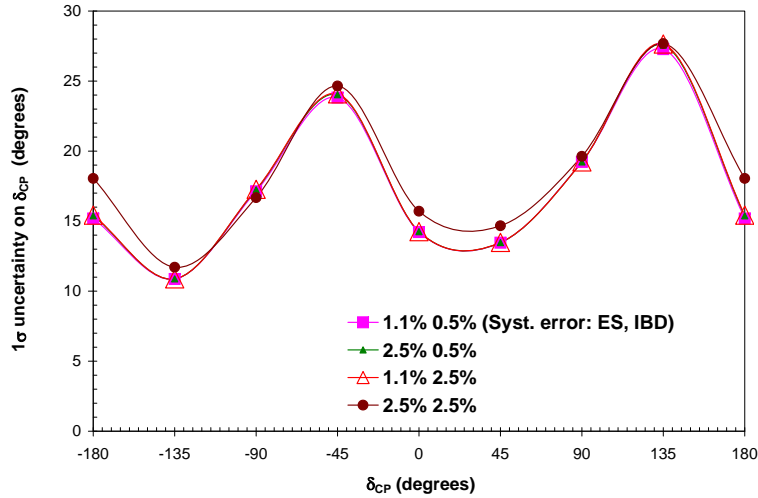


Figure 2.7: The DAE δ ALUS result is insensitive to the input systematic errors. In this study, we vary the magnitude of the input systematic uncertainties (these are the systematic uncertainties prior to the fit). For clarity, we consider only two of the errors ES and IBD (see text for details).

Systematic uncertainties are constrained by pull-term contributions of the form $(k_i - 1)^2 / \sigma_i^2$, where σ_i^2 are the uncertainties given in Table 2.1, for the oscillation parameters and Table 2.3, for the experimental expectations. The χ^2 minimization is performed using the MINUIT program [46].

The DAE δ ALUS sensitivity is shown in Fig. 1.3. Information on the sensitivity is also tabulated in Table 2.4 (top), while Table 2.4 (bottom) tabulates the sensitivity considering only the statistical uncertainty. Thus, one can see that the DAE δ ALUS measurement is statistics-limited. Another way to present the DAE δ ALUS sensitivity is to consider the sensitivity for observing a non-zero value for θ_{13} at the 3 and 5 σ confidence level (CL) for Phase-1 (5-year) running and Phase-1+2 (10-year) running. This result

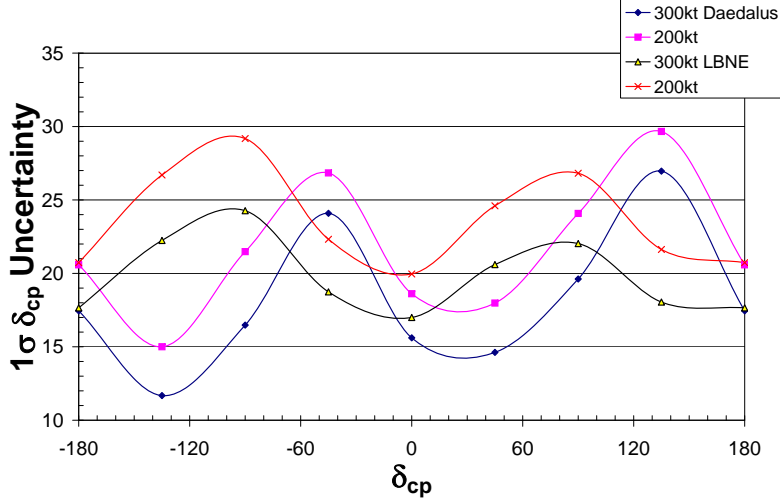


Figure 2.8: The DAE δ ALUS result is sensitive to the statistical uncertainty in the experiment. In this study, we show how the analysis result changes with detector mass. Blue (Magenta) — DAE δ ALUS 300 (200) kton, Black (Red) — LBNE 300 (200) kton.

depends upon δ_{CP} because the level of CP modulates the number of events in the sample (see Fig. 2.3). The DAE δ ALUS expectation is shown in Fig. 2.6. This sensitivity meets that of LBNE, but is inverted with respect to its δ_{CP} dependence [2]. This result is because DAE δ ALUS is an antineutrino experiment while the strength of LBNE is in its neutrino data set.

The final result, after fitting, is insensitive to the input systematic errors. This is because the constraints from the fit to ν -electron and ν_e -oxygen events from the three accelerators are strong. We illustrate this in Fig. 2.7, which presents the 1σ uncertainty on δ_{CP} from the final fit as a function of the value of δ_{cp} . The magenta curve (with squares) shows the result using the standard input errors (reported in Tab. 2.3). To examine the sensitivity of

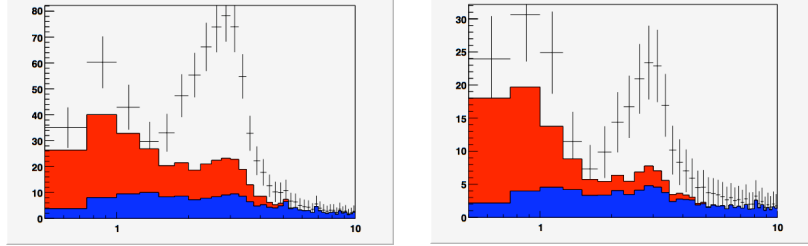


Figure 2.9: Expected events, as a function of energy in GeV, for the LBNE experiment with a 300 kton water Cherenkov detector at 1300 km for ν (5 yr) + $\bar{\nu}$ (5 yr) running (see text for details). Black points — rate with statistical error for $\sin^2 2\theta_{13} = 0.04$, $\delta_{CP} = 0^\circ$, and a normal hierarchy. Red — total background. Blue — intrinsic electron-flavor neutrino background. Left: $\nu_\mu \rightarrow \nu_e$ running; Right: $\bar{\nu}_\mu \rightarrow \bar{\nu}_e$ running.

the result to the magnitude of each input uncertainty, we arbitrarily increase each systematic error, in turn. For example, the effect of increasing the elastic scattering (ES) rate error from 1.1% to 2.5% is indicated in Fig. 2.7 by the green line (with solid triangles). In fact, the new fit result, is so similar to the original fit (magenta line) that it is difficult to see on the plot. This is because the data strongly constrains the fit, so that the input systematic error is not very important. As a second example, we return the ES error back to its original value of 1.1% and increase the error on IBD event rate from 0.5% to 2.5%. The resulting new fit, indicated by the red line (with open triangles), is also in excellent agreement with the original (magenta line) result. In order to see a small but clear effect in Fig. 2.7, one must substantially increase both the ES and the IBD errors to 2.5%. This slightly weakens the constraint from the data and the result is the brown curve (with closed dots).

In contrast to the case of the systematic error, the DAE δ ALUS result is very sensitive to the statistical errors in the experiment. In order to illustrate this sensitivity, Fig. 2.8 compares the DAE δ ALUS 1σ errors in δ_{CP} for the 300 kton detector to a 200-kton detector. Even at 200 ktons, DAE δ ALUS

maintains $> 3\sigma$ capability across a wide range of values of δ_{CP} . For comparison, LBNE is less affected by a loss of statistics, because it is limited by systematics. However, the $> 3\sigma$ coverage at 200 ktons is less.

2.3 A Joint Analysis With the Fermilab Beam

The DAE δ ALUS high-statistics antineutrino data can be combined with LBNE neutrino-only running data to give a sensitivity for observing and measuring θ_{13} and δ_{CP} which far exceeds either experiment alone, as well as the Project X expectation [8], and approaches that of the most sensitive superbeam facilities [10]. In this section, we describe the presently planned LBNE sensitivity, which is based on equal neutrino and antineutrino running. For simplicity, we use the normal hierarchy as our example. We then explain what is gained by running LBNE in neutrino-only mode simultaneously with DAE δ ALUS. The results presented here are in agreement with Ref. [9], once differences in the proposed design are taken into account.

2.3.1 LBNE Current Plans: ν (5 yr) + $\bar{\nu}$ (5 yr) Running

The current plans for the long baseline neutrino experiment from Fermilab to DUSEL (LBNE) are as follows. LBNE proposes to use a wide band neutrino beam, in the range of about 300 MeV to about 10 GeV [47]. This allows the LBNE beam, which is produced at a distance of 1300 km from the detectors at DUSEL, to potentially observe both the oscillation maximum at about 3 GeV and the second maximum near 0.9 GeV. To be specific, the LBNE flux files used in this discussion are:

- `dusel120e250i002dr280dz1300km_flux.txt` (neutrino flux)
- `dusel120e250ni002dr280dz1300km_flux.txt` (antineutrino flux)

This is a 120-GeV, proton-on-target, on-axis, NuMI-like beam with a 280-m decay, designed to reduce the high-energy tail above the first oscillation maximum. This optimization is important because high-energy neutrinos produce single and multiple neutral-current π^0 mesons, which decay to produce electromagnetic showers that are the primary misidentification background in a beam of this type.

We refer to the standard LBNE run as “ ν (5 yr)+ $\bar{\nu}$ (5 yr).” This is defined to be 3×10^{21} POT in neutrino mode and 3×10^{21} POT in antineutrino mode.

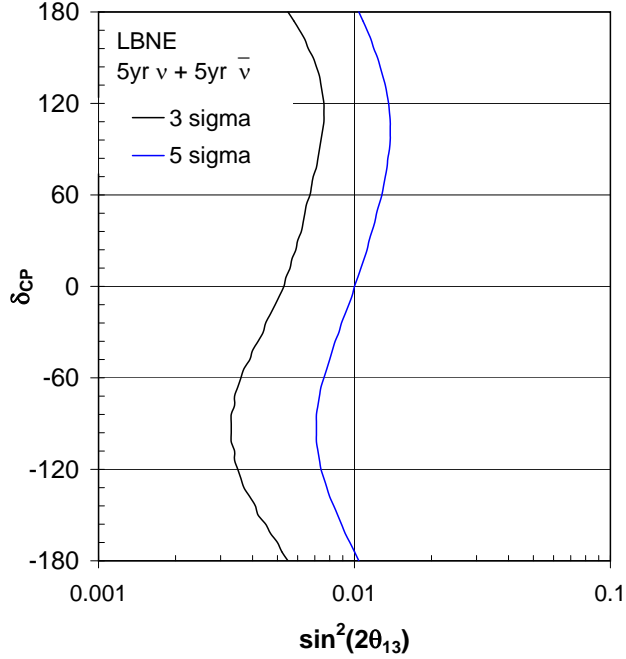


Figure 2.10: The 3σ and 5σ confidence-level exclusion limits for determining a non-zero value for θ_{13} as a function of $\sin^2 2\theta_{13}$ and δ_{CP} , normal hierarchy, assuming ν (5 yr) + $\bar{\nu}$ (5 yr), with the efficiency and uncertainties given in the text.

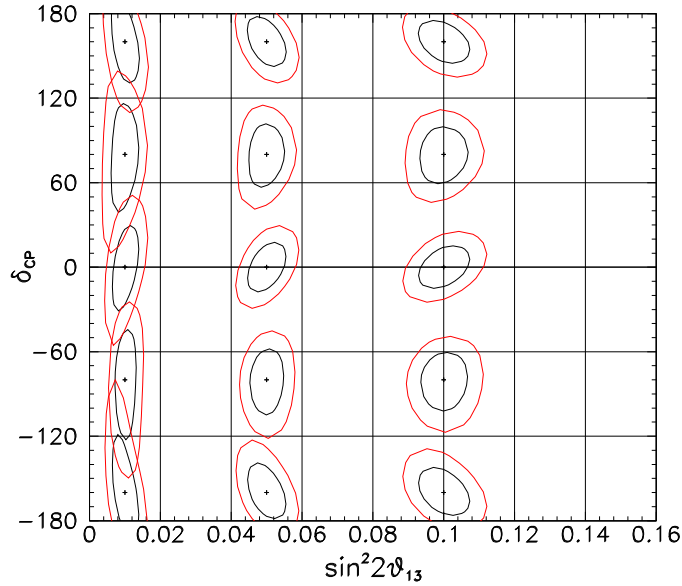


Figure 2.11: Estimates of the uncertainty for a correlated measurement of $\sin^2 2\theta_{13}$ and δ_{CP} at 1σ and 2σ , normal hierarchy, assuming ν (5 yr) + $\bar{\nu}$ (5 yr). The efficiency and uncertainties are given in the text. Sensitivity is for the optimized 120-GeV beam, discussed in the text.

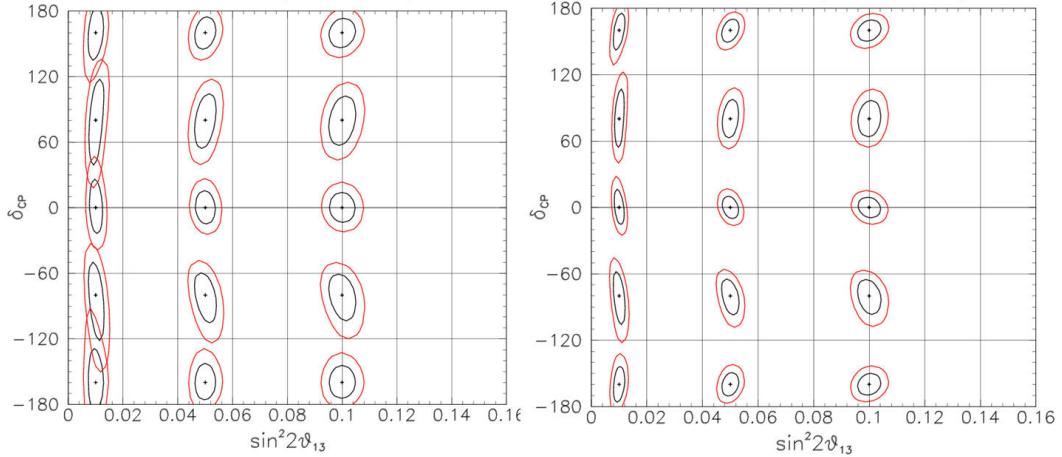


Figure 2.12: The estimated measurement uncertainty for a correlated measurement of $\sin^2 2\theta_{13}$ and δ_{CP} at 1σ and 2σ for the DAE δ ALUS-plus-LBNE, ν -only scenario. Compares a 5-year (left) and 10-year (right) run. Normal mass hierarchy is assumed for LBNE. (Right plot is the same as Fig. 1.5).

If Project X is not in place for the initial run of LBNE, which is planned to begin in 2021, then Fermilab is expected to provide 6×10^{20} POT per year. As a result, this running will require 5 years in neutrino mode and 5 years in antineutrino mode.

Figure 2.9 shows the event rates for LBNE ν (5 yr) + $\bar{\nu}$ (5 yr) for the 300 kton water Cherenkov detector. The points show the expected signal for $\sin^2 2\theta_{13} = 0.04$, and $\delta_{CP} = 0^\circ$ for neutrinos (left) and antineutrinos (right). As seen from these figures, the mis-identification background, shown in red, is substantial, especially for the lower energy second maximum. In addition, there is also a sizeable intrinsic electron (anti-)neutrino contamination, shown in blue, under the first maximum peak.

An issue for the LBNE ν (5 yr) + $\bar{\nu}$ (5 yr) plan is that the antineutrino event rate is low and has a very poor signal-to-background ratio. The rates are low due to the low production rate of the π^- mesons from the primary protons and because the antineutrino cross section is a factor of two lower than the neutrino cross section at 3 GeV. The antineutrino analysis is further complicated and diluted by the high neutrino content of the beam during antineutrino running. For example, in the region between 2 and 5 GeV, 20% of the oscillation events are from $\nu_\mu \rightarrow \nu_e$ instead of $\bar{\nu}_\mu \rightarrow \bar{\nu}_e$.

In order to estimate the sensitivity for measuring θ_{13} and δ_{CP} for the ν (5 yr) + $\bar{\nu}$ (5 yr) scenario, we assume a 15% reconstruction efficiency and systematic uncertainties of 1% for the neutrino/antineutrino flux, 10% for the background, and 5% for the density along the flight path. With these assumptions, the θ_{13} observation sensitivity is given in Fig. 2.10. The correlated measurement precision for θ_{13} and δ_{CP} is shown in Fig. 2.11. These sensitivities can be compared to those of DAE δ ALUS shown in Figs. 2.6 and 1.3. This leads to the conclusion that the two experiments, DAE δ ALUS and LBNE, are comparable in sensitivity and complementary in their regions of best precision.

2.3.2 DAE δ ALUS+LBNE (ν Only)

The complementarity of the two experiments suggests that a combination of the two should give improved sensitivity and precision. In fact, combining the DAE δ ALUS antineutrino data with an LBNE, neutrino-only data set gives a significantly improved oscillation sensitivity and measurement capability. The high-statistics, low-background DAE δ ALUS antineutrino data sample takes the place of the limited LBNE antineutrino sample. In addition, the DAE δ ALUS samples bring in a sample with no matter effects and multiple distances that exploit the on and off-maximum terms in Eq. 2.4. The LBNE data are sensitive to mass hierarchy through matter effects, and for the study below, we assume a normal hierarchy.

LBNE and DAE δ ALUS can take data simultaneously because the two data sets are in well-defined energy ranges that do not overlap. Two scenarios are considered:

- DAE δ ALUS+LBNE ν —5 yr: A five-year run of both experiments, combining DAE δ ALUS Phase 1 with a 30×10^{20} POT ν -only LBNE data set.
- DAE δ ALUS+LBNE ν —10 yr: A ten-year run of both experiments, with the Phase 1 + 2 DAE δ ALUS sample combined with a 60×10^{20} POT ν -only LBNE data sample.

The 1σ measurement uncertainties on δ_{CP} for various scenarios are given in Table 2.5 for an assumed value of $\sin^2 2\theta_{13} = 0.05$. As seen from the table, the DAE δ ALUS+LBNE ν —5-yr scenario does better than either the DAE δ ALUS Phase 1+2 or LBNE ν (5 yr) + $\bar{\nu}$ (5 yr) measurements. The

	δ_{CP}	-160°	-80°	0°	80°	160°
LBNE ν (5 yr) + $\bar{\nu}$ (5 yr)		24.5	31.6	21.3	30.8	21.6
DAE δ ALUS Phase 1+2		17.7	25.3	19.6	23.6	27.2
DAE δ ALUS+LBNE ν -5 yr		16.8	23.7	15.3	25.5	15.0
DAE δ ALUS+LBNE ν -10 yr		10.6	16.2	10.1	17.3	10.4

Table 2.5: The 1σ measurement uncertainty on δ_{CP} for various scenarios and $\sin^2 2\theta_{13} = 0.05$, normal hierarchy. The uncertainties are given in degrees and a normal hierarchy is assumed.

DAE δ ALUS+LBNE ν —10-yr combination reduces the measurement error by a factor of two with respect to the single technique measurements.

The 3σ θ_{13} discovery potential for the various scenarios is shown in Fig. 1.4. The complementarity of DAE δ ALUS and LBNE leads to an excellent $\sin^2 2\theta_{13}$ sensitivity down to 0.002, that is almost independent of δ_{CP} . Finally, the outstanding correlated measurement capability of the combined experiments is as shown in Fig. 2.12. This capability is comparable to the most ambitious superbeam facilities (see [10], Table 5 and Fig. 60).

2.3.3 Comparing to Project X

The Project X proposal at Fermilab would supply 100×10^{20} protons on target to the LBNE beamline in a 5 year time period [8]. We assume a “Project-X scenario” for LBNE which has a 5 year run in neutrino mode, followed by a 5 year run in antineutrino mode. We use a normal mass hierarchy for this study.

The DAE δ ALUS+LBNE ν —10-yr expectation is substantially better than the Project X scenario. This can be seen in Fig 2.13, which gives the total coverage over which a measurement of δ_{CP} can be distinguished from 0 or 180° . The solid red line is the DAE δ ALUS+LBNE ν —10-yr scenario. The solid line with \times s is the Project X scenario. Also shown are the standard DAE δ ALUS and standard LBNE sensitivities. Fig. 1.6 provides similar information, in the form of the fraction of δ_{CP} space which is covered by the four scenarios.

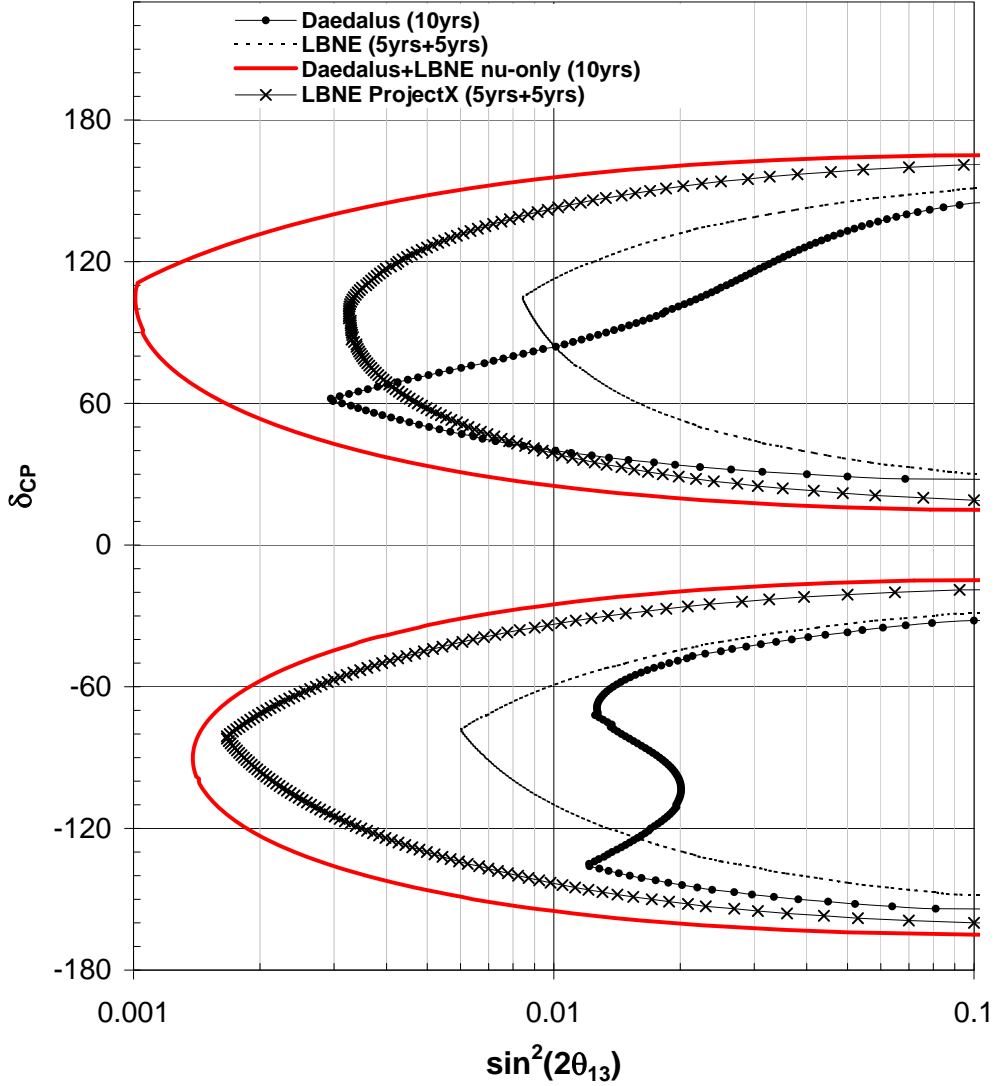


Figure 2.13: The region in δ_{CP} and $\sin^2 2\theta_{13}$ space over which a measurement can be differentiated from 0 or 180° at 3σ . Red solid: DAE δ ALUS+LBNE ν —10 yr scenario, Dashed with \times : Project X scenario. Expectations for standard running for DAE δ ALUS (solid line with dots) and LBNE (dashed) are also shown. Normal mass hierarchy is assumed for LBNE.

2.4 Physics with a Near Accelerator

The DAE δ ALUS near-accelerator will provide a high intensity source of decay-at-rest neutrinos in the 0-50 MeV energy range. Because of the intensity of the neutrino source, many additional physics topics besides the search for CP violation in the lepton sector become available. There are two basic experimental situations possible: physics with the gigantic Gd-doped water Cherenkov detector that will be used for the CP violation measurement and physics that could be done with a dedicated detector on the 300 foot level.

We briefly consider several physics topics accessible with the DAE δ ALUS near accelerator flux. For each topic, we discuss briefly the physics issue and in some cases consider briefly the detector requirements. This is not meant to be a rigorous study but rather a sampling of the breadth of topics made available by the intense DAE δ ALUS flux.

2.4.1 Coherent neutrino-nucleus scattering

Although the process has never been observed before, coherent neutrino-nucleus elastic scattering has the highest theoretical cross section in this energy range by about an order of magnitude. The non-observation is a result of the low momentum transfer characteristic of this type of interaction. Typical nuclear recoil energies for this interaction fall in the \sim 0-100 keV range for medium-A nuclei.

Neutrino-nucleus coherent scattering is an unobserved Standard Model process and as such, is interesting to pursue. Furthermore, any measured deviation from the well-predicted Standard Model expectation could be a sign of new physics. Neutrino-nucleus coherent scattering is also relevant for supernova-burst neutrino detection in terms of oscillation physics and supernova dynamics and evolution. Approximately ten neutrino-nucleus coherent events on argon in a ten second window per ton for a galactic core-collapse supernova at ten kiloparsecs are expected [48]. These neutral-current, flavor-blind, events could provide much-needed information about the $\nu_\mu/\bar{\nu}_\mu$ and $\nu_\tau/\bar{\nu}_\tau$ supernova flux that is out of reach for conventional neutral-current-blind (at low energy) neutrino detectors.

A dedicated coherent neutrino-nucleus scattering detector will be required in order to make precision measurements of this process. A noble liquid detector is envisioned at a distance of 10-50 m from the DAE δ ALUS near-

accelerator neutrino source. Assuming 4×10^{22} /flavor/year, a nuclear recoil energy window from 20-120 keV (30-160 keV), a 1000 (857) kg LAr (LNe) target, and a baseline of 30 m, there will be about 9050 (3700) neutrino-nucleus coherent events/year in the detector. These event rates have been found scaling from the CLEAR proposal [49].

As for direct dark matter searches, cosmic-ray and intrinsic steady-state backgrounds are a significant worry for a coherent neutrino-nucleus measurement. A dedicated coherent detector will enjoy the advantage of a beam window for background estimation and rejection and employ standard WIMP detector background mitigation techniques. The DAE δ ALUS accelerator cycle allows a study of the steady state rate and reduction of the background by 80% simply by the duty factor. The detector design and underground location can further improve background rejection.

2.4.1.1 Measurement of $\sin^2 \theta_W$

Measuring the absolute cross section of neutrino-nucleus coherent scattering can provide sensitivity to the weak mixing angle. A cross section measurement with $\sim 10\%$ uncertainty gives a $\sin^2 \theta_W$ uncertainty at a typical Q value of 0.04 GeV/c of $\sim 5\%$ [50]. Although a first generation experiment may not be competitive with precision atomic parity violation and e-e scattering experiments, it is worth noting that there are no other neutrino-based measurements near $Q \sim 0.04$ GeV/c. Furthermore, the only neutrino-based $\sin^2 \theta_W$ measurement (NuTeV) found a value 3σ away from the Standard Model prediction [51]. As for the weak mixing angle, planned and existing precision measurements are not sensitive to new physics specific to neutrino-nucleus(on) interactions. An absolute cross section measurement consistent with the Standard Model prediction with $\sim 10\%$ uncertainty would provide non-standard neutrino interaction limits more sensitive than current limits by more than an order of magnitude [50].

2.4.1.2 Non-standard interactions

As mentioned previously, coherent neutrino-nucleus scattering can be used to search for new physics in the neutrino sector[52]. One can add to the standard model Lagrangian an extra term of the form[53]:

$$- \mathcal{L}_{\text{NSI}}^{\text{eff}} = \epsilon_{\alpha\beta}^{fP} 2\sqrt{2}G_F (\bar{\nu}_\alpha \gamma_\rho L \nu_\beta) (\bar{f} \gamma^\rho P f), \quad (2.7)$$

where f is a first generation SM fermion: e, u or d , and $P = L$ or R . Such non-standard interaction (NSI) terms can naturally appear when adding neutrino mass into the standard model[54] or from super-symmetry [52]. Thus a diverse range of new physics can be included through the effective parameter $\epsilon_{\alpha\beta}^{fP}$ and constrain using neutrino scattering data.

2.4.1.3 Additional processes

There are additional motivations for new measurements. For example, the nuclear neutron form factor can be linked to neutron star radii, and one might measure this through neutrino-nucleus coherent scattering [55]. Also coherent scattering is a process that occurs during stellar collapse and precise measurements would be useful input to models.

Electron capture on nuclei occurs during stellar collapse, and measurements of the reverse process, neutrino capture on nuclei, should elucidate this mechanism [56, 57, 58]. However, electron capture occurs at lower energies than are available from a stopped pion source, and extrapolation to lower energies could be problematic.

2.4.2 Measurements useful for astrophysics

Because of their copious production rates in astrophysical bodies, neutrinos play a large role in many astrophysical processes. However, poor neutrino interaction cross-section measurements on many nuclei inject significant uncertainty into predictions for rates and kinematics of many astrophysical models, especially stellar processes including supernova explosion and nucleosynthesis[59].

2.4.2.1 Supernova detectors

Supernova neutrino detectors currently suffer from large uncertainties in neutrino-nucleus cross section measurements, and would benefit significantly from new measurements in the relevant energy region on appropriate nuclear targets. Such measurements are needed to understand the distribution of strength in the nucleus. Often, the lower lying strength, e.g. IAS and Gamow-Teller, can be studied using other methods, but the higher order

multipoles, e.g. first forbidden, are more uncertain [60]. This resonance can have a substantial contribution to the cross section.

Any nucleus that is used as a target in supernova neutrino detectors would be useful to measure. In addition, measurements on nuclei in roughly the same mass region would improve supernova neutrino event rate predictions.

2.4.2.2 Nucleosynthesis

There are two types of nucleosynthesis for which cross section measurements are needed. The first is the neutrino process. In this process supernova neutrinos spall neutrons and protons off pre-existing nuclei in the outer layers of the star that is undergoing a supernova explosion. Therefore, all the nuclear yields depend sensitively on the neutrino spallation cross sections. Some of the relevant nuclei are light, so measurements on light nuclei would improve the model predictions.

The other process for which new measurements are needed is nucleosynthesis from hot outflows, e.g. supernovae, gamma ray bursts or compact object mergers. There has been some recent work on light p nucleosynthesis showing that neutrino interactions on protons in relatively late stages have a large impact [61, 62]. Therefore, the neutrino flux will cause some rearrangement in the abundance pattern through neutrino-nucleus interactions. For another type of nucleosynthesis, the r-process, something similar was shown in the mid-nineties: the abundance pattern is rearranged due to neutrino nucleus interactions [63, 64]. For both these processes the nuclear astrophysics community is interested in nuclei much larger than iron, so measurements on heavy nuclei are desired.

2.4.3 Neutrino magnetic moment

A more specific example of neutrino NSI is the case of electromagnetic couplings [65]. Electromagnetic interactions in neutrino-electron elastic scattering, $\nu e \rightarrow \nu e$, can be written in terms of the neutrino energy, E_ν , and the recoil energy of the electron, T :

$$\left(\frac{d\sigma}{dT}\right)^{EM} = \frac{\pi\alpha^2\mu_\nu^2}{m_e^2} \left[\frac{1 - T/E_\nu}{T}\right]$$

where μ_ν is the neutrino magnetic moment, which is usually expressed in units of Bohr magnetons, $\mu_B = e/2m_e$. The current best limit on the muon

neutrino magnetic moment comes from the LSND experiment, $\mu_{nu}(\nu_\mu) < 6.8 \times 10^{-10} \mu_B$ [36]. With the DAE δ ALUS flux, a 1 ton detector at a baseline of 20 m could expect to observe 3 νe elastic scattering events from the weak interaction and three from EM interactions near 1 MeV recoil energy in a one year run if $\mu_{nu}(\nu_\mu) = 1.0 \times 10^{-10} \mu_B$.

2.4.4 Measurement of Δs

The contribution of strange quark and antiquark spins (Δs) to the nucleon spin continues to be an open question. In QCD, Δs is connected to matrix elements of axial operators between nucleon states with 4-momentum P and spin S :

$$\langle P, S | \bar{q} \gamma^\mu \gamma_5 q | P, S \rangle = 2MS^\mu \Delta q,$$

where the right-hand side is understood to be at the asymptotic limit, $Q^2 \rightarrow \infty$, while the matrix element on the left-hand side is calculated at zero 4-momentum transfer, $Q^2 = 0$. The same matrix elements also occur in the expressions for the cross sections of elastic lepton-nucleon scattering and in particular play a significant role in neutral-current, neutrino-nucleon elastic (“NCEL”) scattering. The axial term in this cross section can be written as

$$G_A^{NC,p(n)}(Q^2) = \mp \frac{1}{2} G_A(Q^2) + \frac{1}{2} G_A^s(Q^2), \quad (2.8)$$

where the minus sign in the first term is for scattering off protons and the plus sign is for neutrons.

The first form factor above is known, in the $Q^2 = 0$ limit, as the axial coupling constant in neutron β -decay:

$$g_A^{(3)} \equiv G_A(Q^2 = 0) = g_A \approx 1.26.$$

Measurement of the NCEL νN scattering cross section can be used [66] to extract the strange axial form factor $G_A^s(Q^2)$ which, extrapolated to zero, gives the strange axial matrix element Δs :

$$G_A^s(0) \equiv g_A^s = \Delta s.$$

In practice, it is necessary to consider appropriate ratios of cross sections, in order to minimize uncertainties from the neutrino beam flux and detector efficiencies. New efforts to measure this quantity must determine NCEL

cross sections at low-enough Q^2 to minimize uncertainties from the extrapolation to zero, and must have adequate shielding and active vetoing of cosmic rays, especially in an accelerator with high duty factor. In the following, we consider two possible options for extracting this important quantity.

2.4.4.1 Δs in a mineral oil scintillator detector

The method proposed here follows [67]. The quantity of interest is the NCEL cross-section ratio off protons and neutrons

$$R_{p/n} \equiv \frac{\sigma(\nu p \rightarrow \nu p)}{\sigma(\nu n \rightarrow \nu n)}. \quad (2.9)$$

Scattering occurs primarily off nucleons in the C nuclei in the liquid scintillator. As can be seen from Eq. 2.8, G_A^{NC} has a different dependence on G_A^s for protons and neutrons, therefore this ratio is sensitive to the value of Δs . The ratio is clearly insensitive to uncertainties in the neutrino flux. Knockout neutrons can be identified via their capture by a proton in the liquid scintillator with emission of a 2.2-MeV photon, which then converts and produces scintillation light that can be detected in a photomultiplier-tube array. A capture likelihood ratio can be formed using information on the distance in time and space of the photon signal from the primary hadron and the PMT multiplicity. This is then compared to a Monte Carlo simulation for the same variable and for different values of the quantity of interest Δs , allowing a determination of the most likely value of Δs .

Since the target protons and neutrons are bound, nuclear effects must be considered. However, nuclear corrections have been shown theoretically to be small, expected to contribute about 0.03 to the extracted value of Δs [68]. This is due to the isoscalarity of the target nucleus, implying that nuclear corrections largely cancel in the ratio.

2.4.4.2 Δs in a Gd-doped water Cherenkov detector

One can measure the proton-to-neutron ratio of Eq. 2.9 by detecting the nucleon-knockoff reactions

$$\nu + {}^{16}\text{O} \rightarrow \nu + p + {}^{15}\text{N} + \gamma$$

and

$$\nu + {}^{16}\text{O} \rightarrow \nu + n + {}^{15}\text{O} + \gamma$$

in a large water Cherenkov detector, as previously proposed for ORLaND [69]. Events are observed by triggering on the emitted nuclear gamma rays. By doping the water with gadolinium salts, it will be possible to identify neutron-knockoff events via neutron capture in Gd and the accompanying (delayed) gamma rays, while proton-knockoff events will have no delayed γ s. Again, the ratio method cancels most uncertainties due to beam flux, nuclear binding effects (^{16}O also being isoscalar), and final-state interactions.

Chapter 3

Preliminary Design

This chapter provides information on the preliminary design of DAE δ ALUS. We specifically note the challenges. We are in the process of a cost and design study of the accelerators and report three cyclotron-based options here. The detector follows the presently proposed Gd-based design. Lastly, we consider how the accelerators will be deployed, assuming the detector is available in 2021.

3.1 Accelerator Design

DAE δ ALUS requires Megawatt-class ~ 1 GeV accelerators. While superconducting linacs provide the most conservative technology option, space and cost constraints suggest that high-power cyclotrons could be developed that would meet our goals. Three possible options have been identified: the Compact Superconducting Cyclotron (CSC), which accelerates protons; the Multi-Megawatt Cyclotron (MMC), which accelerates H_2^+ , and the Stacked Cyclotron (SC), which accelerates multiple proton beams in one accelerator. All three are designs which are being developed for commercial purposes – the first for active interrogation for homeland security and the second two for accelerator driven systems used to drive subcritical reactors. We have now embarked on a year-long study of these options, as they apply to DAE δ ALUS, to understand the cost, schedule and R&D needs of each machine. At the same time, we do not wish to exclude high power linacs as an option, considering the synergy with other communities and the possibility of cost-sharing for multi-purpose installations.

Several desirable aspects inherent to cyclotrons attract us to this option. First is compactness, minimizing costs for shielding and space, of particular value for the near site where footprint will be an important consideration. Second is that the fixed-energy and continuous beam character of cyclotrons are desirable features for DAE δ ALUS neutrino production, reducing peak-power loads on targets and providing good compatibility with the short-duty-factor beam structure from Fermilab.

In the sections below, we discuss synergistic uses for the accelerators. However, here we note that these accelerators are not well-suited to two common applications for cyclotrons at present – PET isotope production and proton therapy. For the former, one needs intense beams but only at ~ 30 MeV – the optimal energy for isotope production. For the latter, one wants about 250 MeV and very low power compared to the DAE δ ALUS machines.

3.1.1 Overview of Cyclotron Subsystems

In this section, we consider each component of a MegaWatt class cyclotron, to point out the important issues that drive the design. In following sections we describe the specific design options being considered and how each addresses these issues. At the end we discuss a linac that could be an interesting option.

3.1.1.1 Ion Sources and Injection

Producing milliamperes of protons is not an issue. Modern ECR and multi-cusp plasma sources with CW currents up to 100 mA are available with the requisite brightness, duty factor and reliability.

The injection channel into the cyclotron is usually axial at the radial center with magnetic or electrostatic inflection through 90° into the cyclotron plane. At high currents, coupling in all phase-space planes is difficult to avoid because of space-charge forces, potentially leading to large emittance growth and hence greater difficulty in minimizing beam losses. Acceptable emittance growth depends in large measure upon the extraction strategy, as discussed below.

If the magnetic field in the central (injection) region is high, the low-energy beam will turn on a small radius, and designing the inflector so beam is not lost on the first turn is a challenge. Some beam loss is unavoidable, but the design goal will be to limit this loss, to enable high-power beam at extraction and to minimize heating of inflector components.

3.1.1.2 The Magnetic Field

Compactness is desirable, hence the attraction of higher magnetic fields available from superconducting magnets. However, the higher fields also bring complexity. Vertical focusing and isochronicity require spatial variations (referred to as “flutter”) in the magnetic field of factors of two or more. In lower field machines these variations are produced by shaping the iron poles with hills and valleys. However, in compact machines which must go to higher fields ($\sim 10\text{T}$, well above the saturation of iron) the iron pole shapes play only a minor role, geometry of the superconducting coils must provide the required field variations. Even the H_2^+ ring cyclotron will use large, aperture, superconducting magnet coils at fields as high as 4 to 5 T. Using materials with higher saturation points, such as rare-earth metals, may help in the optimization process. This alternative is currently being studied at MIT [70].

3.1.1.3 RF

The accelerating RF source for high-field cyclotrons will fall within the broadcast band, so that basic generating equipment, which is relatively inexpensive and available, can be used. Because of geometric considerations, the MMC and the SC designs each have “interesting” configurations for the RF cavities.

3.1.1.4 Extraction

The question of clean extraction is a design driver for the cyclotrons. Conventional designs place a thin metallic (or carbon) septum between the beam circulating and the beam emerging from an extraction channel. However, if the machine does not good turn-separation¹, losses on the septum will be unacceptably high, leading to high activation and even melting of the septum. Good turn separation comes from high momentum-gain per turn (large change in orbit radius) and very low emittance (effective beam size). The former requires a high voltage (and expensive) RF system and the latter depends crucially on tight control over space charge at injection. For very high extraction efficiency, the beam size plus width of the septum must be smaller than the turn separation. Note that turn separation is related to $\Delta p/p$, thus as p grows, since typically Δp is relatively constant, it becomes increasingly difficult to preserve good turn separation for higher-energy machines.

¹*i.e.*, sufficient separation of the beam orbit on successive turns.

As a result of these considerations, the designs described here each step away from conventional practice to take novel approaches to extraction. The CSC proposes “resonant self-extraction,” a technique in which the beam is conducted through the edge of the magnetic field via a notched-channel in the magnetic poles and perturbation coils. The MMC accelerates H_2^+ because of the simplicity of extraction via stripping foils that dissociate the molecular hydrogen into two protons, whose orbits can be designed to easily leave the inside of the magnet plane. The stacked cyclotron circulates many lower current beams, thus while the whole is high-intensity, each extracted beam is, in itself, low enough intensity for conventional extraction.

3.1.1.5 Vacuum

The vacuum system is not a major design issue. Preliminary evaluation shows that with a vacuum of 2×10^{-8} Torr, the beam losses should be sufficiently low along the total acceleration path, even for the molecular hydrogen beam. The design goal for beam losses is lower than the estimated beam losses at the TRIUMF cyclotron (520 MeV) which accelerates the very weakly-bound H- ion.

3.1.1.6 The Beam Stop

The design of the beam stop, which is the neutrino source, will be partly driven by the extraction scheme. Our design goal is to have each extracted beam be no more than 1 MW (though there may be more than one extracted beam). This limitation keeps the beam stop design within the range of existing stops, including LAMPF/LANSCE and the 3 GeV hadron line at JPARC.

A side benefit of DAE δ ALUS targeting is production of ^3He in the beam stop region. The ^3He can be separated by cooling the air and sold. This has already been done – Los Alamos sells the ^3He produced by LANSCE [71].

3.1.2 Compact Cyclotrons

Compact superconducting cyclotrons are a potentially low-cost accelerator option for DAE δ ALUS. A class of small-footprint, single stage, mA-current, high magnetic field, superconducting cyclotrons (CSCs) are under development at MIT for the Defense Threat Reduction Agency (DTRA).



Figure 3.1: The Monarch 250 Cyclotron is an example of a compact (250 MeV) superconducting cyclotron which can run at 10 T and which uses the technique of resonant self-extraction. This was designed at MIT for proton therapy applications.

While the CSC represents an advance of the state of cyclotron technology, many aspects of its design and operation with ~ 5 to 10 Telsa fields have already been proven:

- The fundamental feasibility of accelerated beams of ~ 10 mA has been established [72, 73].
- Superconducting compact cyclotrons exist [74], including the the K500 and K1200 at Michigan State University, where the “K” parameter resents the maximum proton energy that could be obtained based on magnetic field size and strength (though it should be noted that these machines are used for heavy ions and so, while in principle the K1200 accelerates protons to 1.2 GeV, this has not been demonstrated in practice). The Monarch 250 (running at 250 MeV) was designed at MIT and is now being commissioned. The Monarch 250 is shown in Fig. 3.1.
- The self-extraction technique has been developed successfully for a 10-MeV conventional cyclotron, the Cyclone SEC[75, 76], marketed by

IBA. The Monarch 250, marketed by Still River also relies on a self-extracted beam.

- The high current-density Nb₃Sn superconducting cable, capable of carrying more than 3 kA/mm², is commercially available [77]. This conductor can be used for fabricating compact magnets exceeding 10 Tesla field strength.

The limiting intensity in isochronous cyclotrons depends on 1) the ability to capture a high current beam at low energy, 2) the suppression of beam loss due to resonant instabilities during acceleration, and 3) the ability to extract the beam from the cyclotron without high losses. In a single stage cyclotron, low velocity ions are captured into stable orbits on every RF cycle to yield a continuous wave (CW) accelerator.

The CSC design uses a proton beam. The attractive option of using H⁻ ions, common now for low-energy isotope-producing cyclotrons (a stripper foil converts the H⁻ to a proton, which bends in the opposite direction, facilitating 100% extraction efficiency), is not available for the CSC because of Lorentz stripping. The extra electron is very loosely bound (0.7 eV), and the relativistic transformation of the magnetic field produces a transverse electric field that, if higher than the binding energy over the size of the ion, will cause loss of the extra electron. The highest-energy H⁻ cyclotron is the 18 m radius TRIUMF machine, with a beam energy of 500 MeV and a maximum field strength of 0.5 Tesla. The other possible ionic form for protons, molecular hydrogen (H₂⁺) also allows for high-efficiency extraction via stripping, but requires, as discussed in the next section, larger machine sizes because of the higher rigidity of the beam (with charge-to-mass ratio of 1/2 instead of 1 for protons.)

In any accelerator, space charge forces are largest when the ion velocity is low; but emittance growth continues, though at a reduced rate as the energy increases, throughout the many orbits required to reach the full beam energy. The growth of transverse emittance (and therefore beam size) may be mitigated and somewhat controlled by the horizontal and vertical focusing generated by the “flutter field” design. The longitudinal emittance growth, on the other hand, leads to an energy spread in the beam which after many turns produces filamentation in longitudinal phase space². In addition to

²filamentary structure (or “stringiness” with substantial empty space between) is a problem because it represents a loss of “phase-space density.”

increasing beam size, an undesirable consequence of these emittance growths is the production of beam halos, particles occupying areas in phase-space well outside the central core of the beam.

The halos are especially troublesome at the extraction channel of the cyclotron, where they will most likely be scraped, depositing their energy on the channel edges, causing unacceptable activation or, possibly, mechanical destruction of components. Loss of even 1% of a 1-MW beam will deposit 10 kilowatts of power, enough to cause substantial damage to components.

The most effective way of mitigating these effects is to inject beam at the highest practical energy. This ensures that injected beam has lowest possible emittance. One also aims to accelerate the beam as quickly as possible with a very powerful RF system.

External, axial injection using a well-designed Electron Cyclotron Resonance (ECR) source offers the best option for yielding high-quality beam. ECR sources produce the required beam current with very good emittance, having this source on a platform external to the cyclotron provides good control over injection beam quality and energy. Limits on injection energy will come from the design of the inflection channel; it must bend the beam through 90° into the plane of the cyclotron; and must be small enough so the beam orbit does not strike it on the first turn – a challenge for a high-field cyclotron for which the first radius will be very small.

A high-voltage RF system will not only speedily accelerate the beam through the low energy region where space-charge forces have the greatest effect, but will also provide the best possible turn separation at high energy, necessary for extraction efficiency. For this reason, the conventional approach to building a high power cyclotron is to accelerate the beam as quickly as possible with a very powerful RF system. This strategy has been employed successfully by the world's currently most powerful cyclotron (1.2 MW), the PSI 600 MeV, 15-meter diameter machine in Switzerland [78].

The self-extraction concept has been demonstrated at low energies (10 MeV), and is being developed for the 250 MeV superconducting Monarch machine. This approach must be extended to the 1 GeV region needed for the DAE δ ALUS machine, and must be refined to provide the extremely high extraction efficiency needed (well in excess of 99%).

All of the relevant design issues will be addressed in DTRA-sponsored research at MIT that is aimed at beam parameters very similar to the DAE δ ALUS parameters. This study will determine whether the CSC approach can be driven to high beam energy and high intensity. In a separate

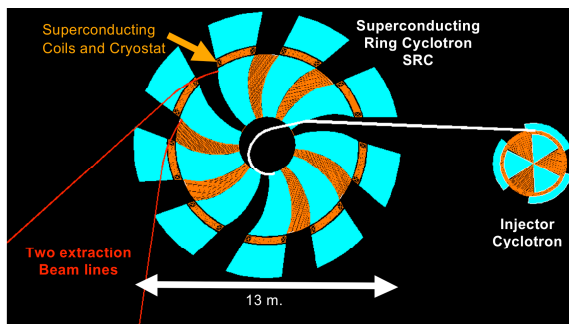


Figure 3.2: Schematic of the Multi-MegaWatt Cyclotron

project members of the DAE δ ALUS collaboration have proposed to build a 1 MeV electron model of a high intensity (2.5 mA) cyclotron. This very low cost device would use an eight sector design to explore all the space-charge physics and extraction issues of a single-stage CSC.

In the case of the CSCs, we would envision implementing cyclotrons which are 1 MW each. Thus, for the Phase 1 scenario, we would install 1, 2 and 3 cyclotrons at the 1.5 km, 8 km and 20 km sites, respectively.

3.1.3 H_2^+ Cyclotrons

A two-cyclotron system – an injector followed by a superconducting ring – which accelerates H_2^+ ions provides elegant solutions to the injection and extraction issues outlined in the introduction to this chapter. This idea is under development at INFN, Catania, for use as ADS technology [79]. The group at INFN is now involved in adapting their design for DAE δ ALUS use. The concept of the Multi Mega Watt Cyclotron (MMC), which can supply a 1.5 MW beam, for DAE δ ALUS is shown in Fig. 3.2. Preliminary parameters of the injector cyclotron and of the superconducting ring cyclotron are also presented in Tab. 3.1.

The cyclotron complex consists of an injector cyclotron, which will accelerate the H_2^+ beam (a hydrogen molecule with just one electron) from the

Superconducting Ring Cyclotron			
E_{inj}	34 MeV/n	E_{max}	800 MeV/n
R_{inj}	1.4 m	R_{ext}	4.5 m
$\langle B \rangle$ at R_{inj}	1.2 T	$\langle B \rangle$ at R_{ext}	2.17 T
sectors	9	Accel. Cavities	6
RF	53.7 MHz	Harmonic	6th
V-peak	220 kV	$\Delta E/\text{turn}$	1.950 MeV
ΔR at R_{inj}	15 m	ΔR at R_{ext}	2.7 mm
Injector Cyclotron			
E_{inj}	50 keV/n	E_{max}	34 MeV/n
R_{inj}	5.5 cm	R_{ext}	1.4 m
$\langle B \rangle$ at R_{inj}	1.2 T	$\langle B \rangle$ at R_{ext}	2.17 T
sectors	3	Accel. Cavities	3
RF	26.85 MHz	Harmonic	3rd
V-inj	70 kV	V-ext	180 keV
$\Delta E/\text{turn}$	1080 keV	ΔR at R_{ext}	11 mm

Table 3.1: Parameters of the SRC and of the injector cyclotron . Superconducting Ring Cyclotron

injection energy of about 100 keV (50 keV/n) up to a maximum energy of about 68 MeV (34 MeV/n). An electrostatic deflector performs the beam extraction, from the injector cyclotron. The beam is then injected into the large cyclotron, the Separated Ring Cyclotron (SRC), by a special bending magnet and a further injection electrostatic deflector. The SRC will accelerate the H_2^+ beam up to the maximum energy of about 800 MeV/n. The use of a thin carbon foil (stripper foil) placed at the radius of maximum energy breaks the hydrogen molecule into two independent protons.

Because the H_2^+ and the protons have significantly different magnetic rigidities, the protons escape quite easily from the magnetic field of the cyclotron. Extraction by stripper foil does not require well-separated turns at the extraction radius and allows use of a moderate energy gain per turn during the acceleration process, with a significant simplification of the RF accelerating system. Stripping also allows the extraction of beams with large energy spread (0.5 to 1%), so the beam bunch elongation produced by space charge effects can be more readily tolerated. Lower requirements for power

transferred inside each cavity increases both the reliability and the conversion efficiency from electrical- to beam-power, as well reducing the overall cost of the RF system.

The special duty cycle (100 μ s Beam On, 400 μ s Beam Off) and the high beam power required by the DAE δ ALUS experiment will produce a serious beam loading effect on the accelerating cavities. That is, when the leading edge of the 100 ms beam pulse enters the cavity the sudden draw of power drops the voltage and affects the balance between the electrode and the supply. This beam-loading will produce a voltage and phase instability that must be compensated. This level of compensation must be high if the beam is extracted by electrostatic deflector (PSI solution). This is a much less serious issue if the extraction is, instead, performed by a stripper foil.

The layout shown in Fig. 3.2 is an evolution of the previous INFN design, presented at EPAC 2000 [79]. The main difference is the reduction of number of sectors, from 12 to 9, and also of the extraction radius, from 6 m to 4.5 m, with a relevant cost reduction. These changes are feasible for two reasons. First, the maximum proton energy for DAE δ ALUS is 800 MeV, compared to 1000 MeV in the ADS design. Second, since 2000, RF cavities with double gaps have been designed which achieve voltages as high as 200kV. According to Fig. 3.2, these accelerating cavities have a spiralled shape that matches the shape of the sectors. At the same time the use of only 9 sectors allow to use of RF cavities with an electrode width of about 16° , with a convenient 6th harmonic driving frequency. In this condition the accelerating voltage across a double gap cavity is $V_{max} * 2 * \sin(96/2) = 1.48V_{max}$. Therefore, a double gap cavity driven with a voltage of 200 kV is equivalent to a single gap cavity driven at 300 kV. The greatest advantage of the double gap cavities versus the single gap cavity or pill box cavity is that their ends exceed the injection and extraction radius by only about 10 cm. The pill box cavity, for example, needs an extra length at the entrance and at the extraction side of about 1 m. Moreover, the double gap cavities can be designed to produce an acceleration voltage that increases with radius, while the pill box cavities have their maximum voltage just at the middle between the injection and extraction radius.

The acceleration of H_2^+ requires a magnetic field two times higher than for protons; fortunately this is not a serious problem if superconducting coils are used. Generally, it is quite difficult to achieve the required isochronous field for a ring using superconducting coils wrapped around the iron pole. The more elegant solution is the use of the so-called ‘‘S-coils.’’ These are a pair

of superconducting coils wrapped around the pole/yoke and perpendicular to the median plane, outside of the extraction radius. This solution allows for more free space among the sectors, and for the cryostat of the superconducting coils to be completely in the outer region, without any interference with the cavities and the accelerated beam. Preliminary evaluations by 3D Mafia code were done to verify the feasibility of this Cyclotron.

The injector cyclotron will be designed scaling up the commercial cyclotron TR-30 of the EBCO company (1.2 mA) or the C-30 of the IBA company (1mA). Both of these cyclotrons are able to deliver proton beams at 30M eV and were designed to be compact, and highly efficient. In our case we face the problem of accelerating a beam current which is about 5 time higher, so the space charge effects will be serious. To overcome this problem we plan to inject the H_2^+ beam at energy of 100 keV and to use 3 RF accelerating cavities to minimize the turn number in the injection cyclotron. The use of 3 sectors and of an extraction radius about double that of the commercial proton cyclotrons, allows more room for the RF cavities as well as use of an acceleration voltage higher than 100 kV even at the injection radius. We expect that this cyclotron should be able to deliver a beam current of H_2^+ as high as 5 mA, assuming a 100% duty cycle, or 1 mA with a 20% duty cycle. With respect to the space charge effects, we have to consider that the perveance³ of a proton beam and an H_2^+ beam with the same energy is the same if we work at low energy ($E < 100$ MeV). Therefore, the emittance of a H_2^+ beam at 100 keV is the same or better than the emittance of a proton beam at the same energy. Moreover, proton sources are generally able to produce high beam currents of H_2^+ . In the present case, we need an H_2^+ source able to deliver a beam current of about 33 mA. The injector cyclotron, equipped with a simple buncher, should be able to catch and accelerate about 15% of the injected beam. This means that about 28 mA of H_2^+ beam with an energy of 100 keV (2.8 kWatt) will be lost in the first turn. The effect of this power loss on the superconducting materials needs to be considered, but because of the low energies, this does not result in high activation.

At DAE δ ALUS, for Phase 1, we could install 1, 1 and 2 accelerators at the 1.5 km, 8 km and 20 km locations, respectively. This is slightly different from our base design in that it supplies 1.5 MW, 1.5 MW and 3 MW, respectively.

³The value of perveance is a measure of the significance of space charge effects on the motion of the beam.

	injection	extraction	
Energy	150	800	MeV
hline Radius	3.0	5.0	m
Magnetic Field	1.2	1.4	T
RF Frequency (6 th harmonic)	48		MHz
Number of magnet sectors	8		
Number of RF Cavities	4	6	
Energy gain per turn	4	6	MeV
Radial separation of turns		7	mm

Table 3.2: Parameters of the Stacked Cyclotron

3.1.4 Stacked Cyclotrons

The stacked cyclotron proposal, with parameters summarized in Tab. 3.2, is inspired by the success of the isochronous cyclotron (IC) at the Paul Scherer institute (PSI). The PSI machine was built 35 years ago, and after two generations of upgrades and improvements it routinely delivers 2.2 mA of proton beam at 650 MeV energy. As stated earlier, the challenge in improving upon this performance is in increasing the beam current. The space charge tune shift at injection drives rapid emittance growth, and the separation of orbits at extraction after emittance growth produces large beam loss at the extraction septum.

The Texas A&M University (TAMU) group has invented a novel method to solve these problems, inspired by the needs of the ADS application. They take the established performance of PSI and replicate it in each layer of a flux-coupled stack of superconducting ICs, shown in Figure 3.3 (a). The magnetic configuration follows that developed for the single ring cyclotron at RIKEN[80], in which the field in each aperture of a sector magnet is produced by a pair of cold iron pole pieces on which superconducting windings are bonded. The pole pieces are suspended within a warm-iron flux return, with vacuum gaps above and below, so that the huge Lorentz image forces between the poles and between pole and flux return cancel one another. This approach makes it possible to enjoy the benefits of a superconducting magnet without having to cool the immense thermal mass of the flux return. Figure 3.3 shows a detail of one sector magnet (b) and of one pole piece (c). Assuming the same performance as PSI, a stack of five ICs operating with 800 MeV, 2.2

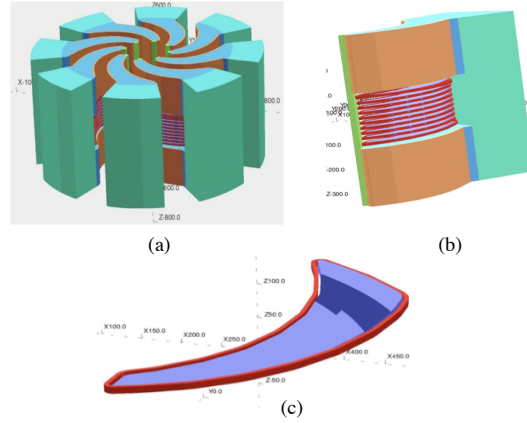


Figure 3.3: The design of the stacked cyclotron. a) The overall design; b) detail of one sector magnet; c) detail of one pole piece.

mA would provide the proton beam needed for DAE δ ALUS. Targeting the five beams in a symmetric pattern on each beam dump should significantly simplify the design and operation of the beam dump by limiting the local energy density. Each element of the flux-coupled IC is, in effect, a close cousin of the PSI IC, except with higher injection and extraction energies, and the use of superconducting magnet coils and superconducting RF cavities.

The design of the superconducting RF cavity was a particular challenge. It operates at 58 MHz (6th harmonic of the cyclotron frequency), and if it were an empty cavity it would be much larger than what is needed to fit within the space between ICs in the flux-coupled stack. The TAMU group invented a dielectric-loaded resonator that fits in the required space, as shown in Fig. 3.4. It should be capable of 1 MV accelerating voltage and excellent mode stability. This is the one element of the flux-coupled IC stack that requires long-lead R&D to design, build, and test a prototype to validate the design.

In related research, the Cyclotron Institute at Texas A&M University operates a superconducting cyclotron complex for nuclear research, and is currently upgrading the complex to re-accelerate radioactive nuclei using its original Cu-coil cyclotron. The Nuclear Engineering Department at Texas A&M University is interested in collaborating with the Accelerator Research

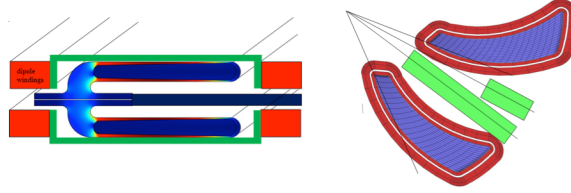


Figure 3.4: Left: Dielectric loaded superconducting cavity (1 MV/turn each); Right Placement showing additional cavity to boost orbit separation at extraction.

Lab to develop ADTC (Accelerator Driven Thorium Cycle) fission. The TAMU group proposes a development scenario in which the accelerator would be built and commissioned at a site near Texas A&M University. Because the parameters of the accelerator are consonant with our long-term objective of ADTC fission, the TAMU group envisages forming a collaboration with our colleagues at the University of Texas and seek funding from the State of Texas with which to construct the physical facilities needed to house and operate the accelerator during development in Texas. Once it were complete and operating, having demonstrated technological feasibility, this prototype could be dismantled and moved to the DUSEL site for use by DAE δ ALUS.

3.1.5 Other Types of Accelerators: Superconducting Linacs

A superconducting linac would be a very conservative option for achieving the high currents needed for good neutrino production. Superconducting RF cavities are now used in many high-current, high-energy accelerators, and while the first of these were electron machines (JLAB, TESLA), the final stage of the SNS Linac constitutes a good example of a proton linac in the GeV range. Furthermore, design studies at Fermilab for Project X, and at MSU and Argonne for the FRIB project have further optimized engineering and costing for this class of linacs.

Injection into a linac is much simpler than for a cyclotron, and front-end designs with over 100 mA of continuous proton current have been demonstrated (the LEDA project at LANL). Apertures inside superconducting cav-

ities are very large, typically 10 cm or more, so beam loss during acceleration is a much easier problem to solve. Extraction is also certainly not the problem it is with cyclotrons. One drawback is the large footprint required. The second, which accelerator physicists are working to address, is the high cost of the systems.

An interesting opportunity might exist for working with the medical-isotopes community for developing a mutually-beneficial design. A serious problem exists in the US today regarding a steady, reliable supply of ^{99}Mo , an isotope used in approximately 50,000 nuclear medicine procedures per day in the US alone. This isotope is abundantly produced as a fission fragment from neutron irradiation of highly-enriched uranium (HEU). There are no reactors in the US capable of supplying the year-round quantity of the isotope required, and considering the problems in the US associated with HEU reactors, this is not likely to change anytime soon. As a consequence, the supply of the isotope comes from three aging reactors, one in Canada (currently shut down) and two in Europe (both facing significant maintenance problems).

An interesting accelerator design has been proposed by the Physics Division of Argonne National Lab, which would use a multi-megawatt proton beam (at an energy close to 1 GeV) to produce neutrons in a heavy-metal blanket that would then bombard a small core of HEU from which the ^{99}Mo would be extracted. The production from this accelerator would be capable of satisfying the entire US demand for the isotope, using less than half of its beam capacity.

3.1.6 Neutrino Source Design

The neutrino source for the DAE δ ALUS experiment will be a beam stop for the proton beam. The beam stop will have a series of important functions, all of which require design considerations. First, the beam stop produces the mesons which in turn either capture without decay, come to rest and decay, or escape the beam stop altogether and decay; all decays produce neutrinos. The design of the beam stop can affect the neutrino flux by altering the relative likelihood of these processes. Second, the beam stop dissipates the ~ 1 MWatt energy of the beam, dissipating it into heat in a controlled fashion. Third, the outer portions of the beam stop contains the significant flux of neutrons and gamma rays produced by interactions of the proton beam with the inner core, of importance not only for personnel

protection but also for limiting dose on nearby equipment and the water table. High-power beam stops for proton accelerators have been designed for a variety of experiments [81, 82, 83, 84, 85], providing significant guidance in all three of these considerations. Each design goal of the beam stop is discussed in turn.

3.1.6.1 Neutrino Flux

The beam stop produces positive and negative pions and no kaons due to the below-threshold kinetic energy of the incident proton beam. With appropriate geometric design, 98% of pions come to rest in the beam stop, with only $\sim 2\%$ escaping laterally or longitudinally [86]. Neutrinos result predominantly from the decays $\pi^+ \rightarrow \mu + \nu_\mu$, $\mu^+ \rightarrow \bar{\nu}_\mu \nu_e e^+$ for pions and muons coming to rest within the beam stop. The charge-conjugate decays are suppressed because all but $\sim 5 \times 10^{-4}$ of π^- are captured on nuclei without decaying, and even the μ^- from the few remaining $\pi^- \rightarrow \mu^- \bar{\nu}_\mu$ decays have an increased likelihood for capture without decay for heavy nuclei [87]. To control the neutrino flux, it is important to reduce or understand the meson leakage from the beam stop which results in decays-in-flight to neutrinos, albeit at higher neutrino energies than those from the stopped pion decay chain, and it is important to reduce or understand the residual decays of non-captured $\mu^- \rightarrow e^- \bar{\nu}_e \nu_\mu$ which produce an anti electron-neutrino background to the oscillation search.

We propose to study a beam stop with an inner core composed of graphite slabs stacked longitudinally along the beam axis. A significant amount of data exists [88, 89, 90, 91] for pion production on nuclei, particularly for carbon. These data, along with information from Monte Carlo simulations [32, 33], indicate that, at a beam energy of 800 MeV, the number of neutrinos produced is $\nu_\mu/p \approx 0.172$, while the ratio $\pi^+/\pi^- \approx 4.5$. Furthermore, the moderate atomic number $Z = 6$ produces a significant capture rate for μ^- , reducing the $\bar{\nu}_e$ contamination in the beam. With better optimization, one should be able to further reduce the wrong-sign neutrino contamination relative to the LANL beam stop.

Design considerations for the beam stop will include possible consideration of larger Z absorber plates embedded in the beam stop to reduce wrong-sign neutrino contamination, and the specification of the lateral dimensions of the beam stop which controls meson leakage and the decay-in-flight component of the beam. Past experiments suggest that the uncertainty in these

components is 2-5% and in the overall neutrino flux is of order 11% [92], so it is of some use to reduce the background fluxes.

3.1.6.2 Thermal Analysis

The conceptual design of a beam dump for pion production from a high-current proton beam has been studied. It consists of a water-cooled stainless-steel or copper tube centered on the beam axis which contains a set of graphite disks or slabs. The disks near the beam entrance have concentric holes forming a re-entrant hole for the beam to spread the beam energy loss into the depth of the dump (see Figure 3.5, left). The energy deposited by the beam in the graphite disks is conducted radially to the surrounding water-cooled lines. Such lines can be shrink-fit to the exterior of the graphite disks, or, as in the case of the NuMI beam stop, the water cooling lines are clamped into the slabs of graphite for thermal contact (see Figure 3.5, right). The re-entrant hole is shaped in such a way as to keep the temperature constant over the re-entrant hole surface assuming constant temperature at the cooling tube. A more sophisticated design in which the cooling tube is tapered radially with respect to the beam axis such as to keep the heat flux density constant over the tube between the beam entrance and the end of the re-entrant hole in addition to keeping the re-entrant hole temperature uniform was also studied.

Assuming a circular double-Gaussian proton beam profile of r.m.s. radius σ and exponential proton energy deposition in graphite with a interaction length L , examples for a cylindrical and a tapered beam dump were evaluated for the following parameters typical for a DAE δ ALUS beam stop: beam power = 1 MWatt, beam radius R.M.S. $\sigma = 5$ cm, graphite density = 1.75g/cm^3 , $L = 50$ cm, diameter of cooling channel = 30 cm, diameter of re-entrant hole=11.4 cm, cooling water = 100°C . The resulting shapes of a cylindrical and a tapered beam dump are shown in Figure 3.6. The total length of the beam stop is constrained by the depths of the re-entrant holes plus the range of protons in graphite (125cm for 700MeV protons). Figure 3.6 shows the result of thermal calculations for the beam stop. As with the NuMI design, the present concept has the advantage of keeping water cooling lines out of the shower profile of the beam [93, 94]. A significant advantage over other beam stop designs, however, is that the re-entrant hole reduces the temperature at the center of the core by spreading out the interactions of the proton beam. To minimize sublimation from the hot graphite

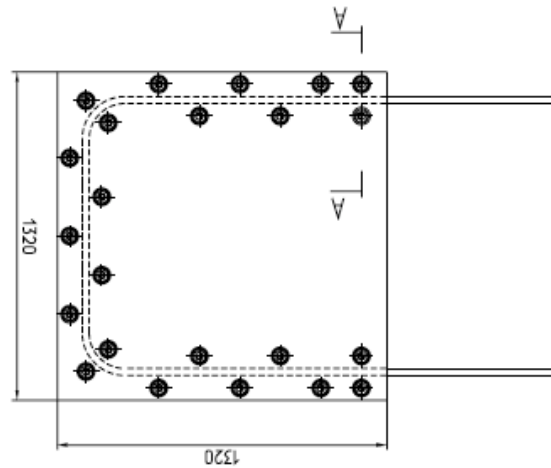
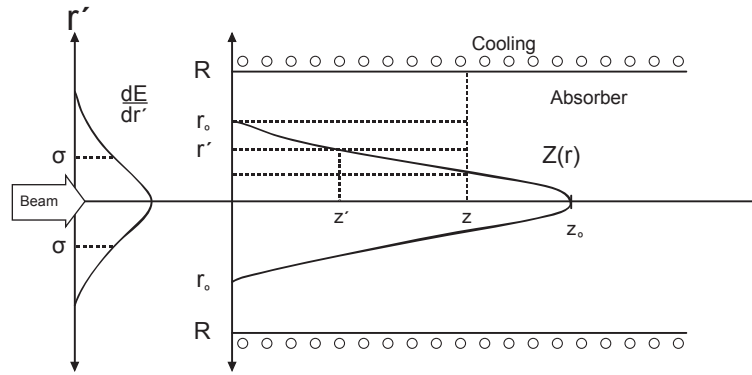


Figure 3.5: (top) Conceptual design of a beam stop with tapered entrance hole for the proton beam. The shape of the entrance hole produces a constant temperature profile along the length of the beam stop. (bottom) Conceptual design from the NuMI beam for establishing thermal contact between the slabs of the beam stop core to water cooling lines kept external to the beam profile which involves sandwiching the cooling lines into channels between adjacent bolted slabs of the beam stop.

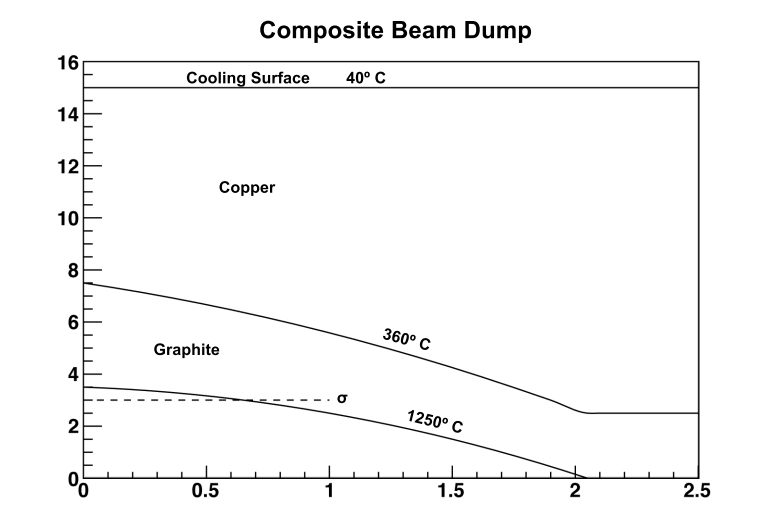


Figure 3.6: Graph of the temperature profile in the beam stop. The vertical axis is the radius away from the beam axis and the horizontal axis is longitudinal depth within the beam stop. Two curves are shown, one at the inner edge of the re-entrant hole which is maintained at a temperature 1250°C and the second at a line of constant temperature 360°C.

slabs, they could be sputter-coated with a few microns of Molybdenum or Tungsten eliminating the need for a beam window.

3.1.6.3 Radiation Protection

A significant design consideration will be the protection of personnel, equipment, and ground water from the radiation produced in the beam stop. It is envisioned that the primary proton beam will be brought to the beam stop through a penetration in a shield wall which separates the proton extraction line from the target station. It is further envisioned that the water-cooled graphite core of the beam stop is embedded in a larger structure of cast steel and concrete shielding blocks for attenuation of gamma rays and neutrons produced in the beam stop. While the containment of the core inside such a larger structure accentuates the need for thermal analysis, it is clear that shielding thicknesses of ~ 1 m of steel and ~ 1 m of concrete is required just to keep residual activity levels to 30 mR/hour after a year of 1 MWatt operation of the beam line [93]. Such will be the subject of simulation and calculation

work during the first year of DAE δ ALUS R&D. An additional concern will be the mitigation of humidity and water in the target station area. A significant experience from operation of the NuMI beam was that high humidity levels due to the below-grade location of the target station causes moisture capture and irradiation in the concrete shielding leading to high levels of tritium [95]. Such humidity requires mitigation by dehumidification systems.

3.2 Detector Design

In designing DAE δ ALUS, we have adhered closely to the proposed large water Cherenkov detector design. As with many of the low energy (<100 MeV) analyses, this experiment requires Gd-doping and benefits from good photocathode coverage. We consider progress on these issues in this section.

3.2.1 Gd Doping

In order to detect IBD events, the DAE δ ALUS detector must be doped with the neutron capture agent gadolinium (Gd). Gd offers two essential advantages over the competing process of hydrogen capture: it reduces the capture time for the neutron generated in the IBD interaction from 200 μsec to about 30 μsec , and the energy release from the capture interaction is higher - 8 MeV compared with 2.2 MeV for hydrogen. These twin benefits provide a clean tag for the time correlated positron and neutron which make up the IBD signal.

Gd-doping is a familiar technology for antineutrino detection, having been implemented in numerous liquid scintillator experiments, including Double Chooz [96], SONGS1 [97], and others. Stable operation over 1 year time scales has been demonstrated in these 1-10 ton scale liquid scintillator detectors.

Though well understood in small (by DAE δ ALUS standards) scintillator detectors Gd-doping has been only partially demonstrated for large water Cherenkov detectors. LLNL has built and successfully operated 1-5 ton scale water detectors doped with 0.1% – 0.2% concentrations of Gd [98]. These detectors have shown both the expected time correlations and the increased energy output from the neutron capture event using tagged neutron (Americium-Beryllium, AmBe) calibration sources. A 250 kg detector also empirically demonstrated the long term compatibility (1 year time scale) of

GdCl₃ compounds with acrylic⁴. Implementation of these detectors is underway for nonproliferation applications that require large solid angle and efficient neutron detection.

In addition to these small scale performance tests, a test was performed at the SuperKamiokande experiment, in which a small sealed vessel of Gd-doped water was lowered to the center of the detector [99]. The vessel also contained a tagged AmBe source, so that the neutron emission time was known to within a few ns. The significance of this test is that the large water volume guaranteed full containment of the Gd-capture gamma-ray shower. By comparing with the well-tuned Superkamiokande energy calibration, it was found that approximately 50% of the shower energy is detectable in the Cherenkov light emission channel. (4.3 MeV of energy out of an available 8 MeV from the capture gamma-ray shower.) The missing energy is a limitation imposed by physics that would be present even with perfect light collection. It occurs because not all of the Compton electrons generated by the gamma-ray interactions are above the 0.78 MeV threshold for Cherenkov light production. In a set of soak tests related to this experiment, the compound Gd₂(SO₄)₃ was found to be most compatible with the structural materials exposed to the water-Gd solution.

While these tests are all encouraging for a large scale Gd-doped detector, important R&D steps remain in order to demonstrate successful operation at the 150,000 ton scale required for DAE δ ALUS (and LBNE). The R&D program is derived from a set of physics requirements defined for the LBNE water detectors, which include a Gd-doping option. The table in Figure 3.7. taken from an LBNE project planning document [100], summarizes these requirements. The requirements are essentially identical to those needed for DAE δ ALUS, though some relaxation of constraints could arise in DAE δ ALUS, due to the different event rates. DAE δ ALUS will consider which if any elements of the LBNE Gd doping strategy would need to be modified on signal to background or cost grounds.

From the physics requirements, a set of research and development priorities have been identified. The steps listed below are part of the larger work plan for the overall LBNE water detector development program. DAE δ ALUS will benefit from the overlap in detector needs of the two proposed experiments.

⁴In this detector, the entire detector interior was constructed of acrylic in order to reduce the likelihood of contamination/clouding from leached materials.

Capacity	5 cavities having 150 kton of water each, or 2 tanks having 150 kton each. a) One Treatment system for filling and recirculating a cavity and b) Separate filling and recirculating systems.	Scientific Competitiveness
Quality	ASTM Type 1 and should include uranium removal and membrane final degasification.	Water transparency to Cherenkov light
Recirculation-only systems	In addition to microfiltration, should have sterilization, de-ionization, degasification, and chiller stages.	Optimize cost, allowing [re]chilling of partially filled cavity
Fill and Recirculation system	Depth Filter, a Carbon filter, a Softener, and a Reverse Osmosis unit, in addition to the stages required for recirculation.	
Recirculation rate	300 gal/min	
Fill rate	250 gal/min	<3 months to fill
Temperature	Achieve a water temperature of 13° C over a 6 month period, which should start at the beginning of the fill. The system should maintain the temperature of 13° C in the steady state operational period after the first 6 months.	Suppress biological growth to maintain transparency and reduce scattering
Dissolved oxygen	<(?) 0.06 mg/liter.	Light transmission
Sterilization	UV treatment	Suppress biological growth
Fill Capacity	130kT per 3 months	Timeliness
Location of Water system	Adjacent to the detector at the 4850 foot level in the Homestake mine.	Reduce system complication
Instrumentation	Sufficient instrumentation so that its health and basic control functions can be accessed remotely	Safety
Drainage	Water Treatment Plant shall have the capability of draining the tanks at a rate of >250 gal/min to a facility supplied pump located on the same level. The draining system shall provide treatment to the water from the tanks so that it can be discharged into the local environment.	Environmental safety
OPTION: Recirculation Rate	600 or 1200 gal/min	Water purity in system may require more frequent cleaning.
OPTION: Th and U removal	The plant should optionally provide uranium and thorium removal to $U < 1.4 \times 10^{-15}$ g/g and $Th < 8.3 \times 10^{-16}$ g/g.	Solar and Supernovae physics neutrino physics.
OPTION: Gd Compound	add 0.2% of Gadolinium compound to the water in the tanks to make the Water Cherenkov Detector sensitive to neutrons. The recirculation system should be able to clean the water to the levels specified above and to return it to the tanks maintaining the Gadolinium concentration. The drainage system should be able to remove the Gadolinium compound from the water when the tanks are drained.	Neutron detection for Solar and Supernovae physics, neutrino physics.

Figure 3.7: A list of basic requirements for the LBNE water systems, including the Gd doping option. This table is extracted from [100]

- demonstration that the water can be purified sufficiently even in the presence of the Gd compound, which would normally be removed in the purification process, and
- demonstration of long term compatibility of all exposed structural materials with the Gd-water solution, and completion of a downselection process for the choice of Gd-bearing chemical compound;
- demonstration that the attenuation length of the water is not compromised directly by the Gd-solution or by leaching from structural materials;
- demonstration of scaling of the Gd purification process, including demonstration that Gd can be kept uniformly dissolved throughout the detector on time scales compatible with the water circulation and purification rate.

The LBNE work plan elements relating to Gd-doped detector R&D are described briefly in the following sections. DAE δ ALUS will join forces with the rest of the LBNE team to support studies of the Gd doping option for the DUSEL WC detectors.

In addition to the US LBNE effort, a 200 ton scale Gd-doped detector and accompanying filtration system is being built in Japan [101]. This detector, known as EGADS, will help answer several of the outstanding questions regarding Gd-doping of detectors.

3.2.1.1 Water Purification in the Presence of Gd

The LBNE collaboration has a significant effort invested in developing a large scale purification system that is compatible with the use of a Gd dopant. The 'standard' purification system for large water detectors, such as that used for the SuperK detector, must be modified to allow introduction of purified Gd after cleaning of the water. A flow chart for one proposed purification method, developed at UC Irvine, is shown in Figure 3.8. The basic idea is to remove a Gd concentrate from the partially cleaned water, pass the Gd-free water through additional purification steps, separately remove Uranium and Thorium contaminants from the Gd concentrate, and recombine the purified Gd concentrate with the purified water. The first elements of this process have been demonstrated in a lab-scale system at UC Irvine. Research is

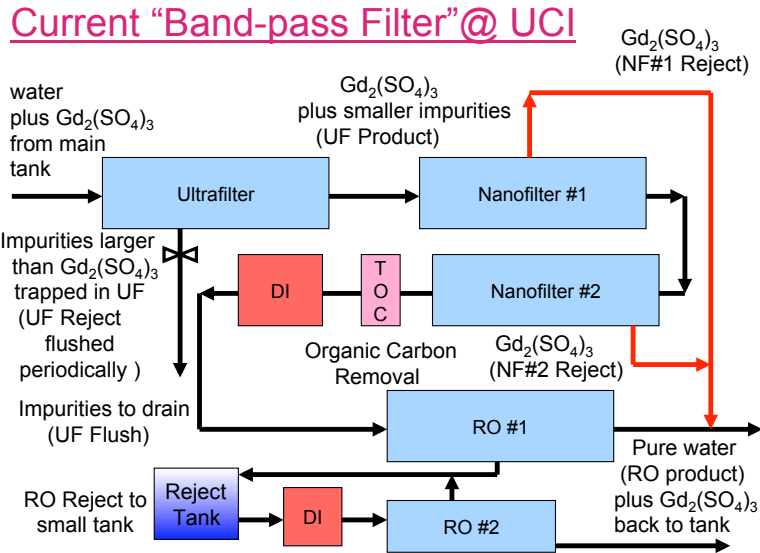


Figure 3.8: A flow chart of a proposed Gd purification and mixing procedure for the DUSEL WC detectors. The basic concept has been developed at UC Irvine.

ongoing at BNL, UC Irvine and elsewhere on the U/TH removal from the Gd concentrate.

3.2.1.2 Materials Compatibility and Attenuation Length Studies

As part of its LBNE activities, Brookhaven National Laboratory (BNL) has developed a list of structural materials likely to be directly exposed to the Gd water in the DUSEL water detectors. LLNL is conducting long term tests of the integrity of this set of materials, and is making 1% accurate measurement of changes in the water attenuation length that may be caused by the introduction of a Gd compound. This precision is sufficient to confirm whether the 100m attenuation length targets for LBNE and DAEδALUS can be met. GdCl₃ and other compounds will be tested. Initial test results demonstrating possible leaching of Fe from stainless steel in the presence of GdCl₃ may be found in [102]

3.2.1.3 Scaling of Water Purification Systems in the Presence of Gd

In addition to defining a process for maintaining water purity in the presence of Gd, the LBNE collaboration is working on the engineering aspects of scaling the system to work with 150 kT mass detectors. Important elements include the throughput of filtration systems and pumps, the specific layout of the DUSEL caverns and water supply lines, and uniformity of mixing of the Gd in the water. Leaks in the detector are also far more important in a Gd-doped detector, because the underground sites will not allow direct discharge of Gd-doped water to drainage systems. Since prior detectors such as Superkamiokande have had water losses, leak tightness must be improved.

The EGADS experiment in Japan will address several of the above R&D questions simultaneously, using a fully functional 200 ton scale detector and selective filtration system. In particular, EGADS goals are to study the rate at which Gd can be introduced into the water, the uniformity of Gd mixing in the water, the Gd removal process, the selective water filtering process, and materials effects in an integrated detector. (It will not directly address the U/Th removal process).

3.2.1.4 Conclusions for Gd Doping and Detector Scaling

The underlying physics of Gd-doped water detectors is now well established. The R&D program described above, is being pursued by LBNE and by the EGADS experiment in Japan. The program directly addresses the outstanding engineering questions that must be answered in order to achieve 150 kton operation of a Gd-doped detector.

3.2.2 Photocathode Coverage

In terms of photocathode coverage, DAE δ ALUS' requirements are motivated in principal by the need for efficient triggering at low visible energies, accurate energy reconstruction, and accurate reconstruction of the out-going lepton scattering angle. Efficient triggering and vertex reconstruction is necessary to observe the 8 MeV gamma cascade from the neutron capture on Gd characteristic of the IBD signal. Further, since the size of the δ_{CP} conversion effect in Eq. 2.3 is coupled to the amount of interference between the two neutrino mass splittings, accurate energy reconstruction is important to extract

δ_{CP} . Good angular resolution is essential for distinguishing the two dominant normalization event samples from one another. The Super-Kamiokande experiment's first (SK-I) and second (SK-II) run periods provide an instructive example of the capabilities of a large water Cherenkov detector at < 100 MeV energies with differing photocathode coverages: 40% and 19%, respectively. Numbers in the discussion below for SK-I are taken from [103] and those for SK-II are from [104].

Super-Kamiokande has demonstrated efficient triggering at low energies in both of the above run periods. At 40% photocathode coverage, SK-I collected 7 PMT hits per MeV of total energy (kinetic energy plus rest mass energy) and triggered with 100% efficiency down to 4.5 MeV. SK-II similarly triggered at 100% efficiency above 6 MeV with half as many hits per MeV. Note that these thresholds are below the minimum visible energy requirement for both IBD positrons (20 MeV) and recoil electrons (10 MeV) from $\nu - e$ scattering. This is below the total energy of the gamma cascade from neutron capture on Gd, often the cascade energy is partitioned among several gammas, with one or more receiving less than 2 MeV. The least energetic gammas are not likely to result in Compton-scattered electrons above Cherenkov threshold, and not all of the gamma energy is observed. For this reason, the mean observed energy of Gd capture events is shifted down to 4.3 MeV [4], where the trigger efficiency of SK-II was only 30%.

As discussed in Sec 2.2.2 the recoil electron direction in $\nu - e$ scattering events is strongly peaked in the forward direction. Electrons emitted in $\nu_e - O$ scattering, on the other hand, have a weaker angular dependence. At DAE δ ALUS energies the $\nu - e$ scattering peak can be isolated by selecting scattering angles within 26° of the beam direction (see Sec. 4.1), so angular resolution in the water Cherenkov detector that is better than this value is desirable. During the SK-I run period the angular resolution of recoil electrons was found to improve from 27° at total energies of 10 MeV to 23° at 15 MeV. With decreased photocathode coverage in SK-II the resolution at 10 MeV was 30° and fell to 25° at 13 MeV. Both photocathode coverages lead to resolutions near the required threshold in the energy range of interest and generally improve to a plateau near the IBD positron minimum energy

Despite the relative stability of the above variables against lower photocathode coverages, the vertex and energy resolution of the detector are more sensitive to less photon collection. At 5 MeV of total electron energy, the SK-I (SK-II) resolution is 18%(28%) and improves to 12%(16%) at 20 MeV. The vertex resolution at 5 MeV was 150 cm (210 cm) and 70 cm (100 cm)

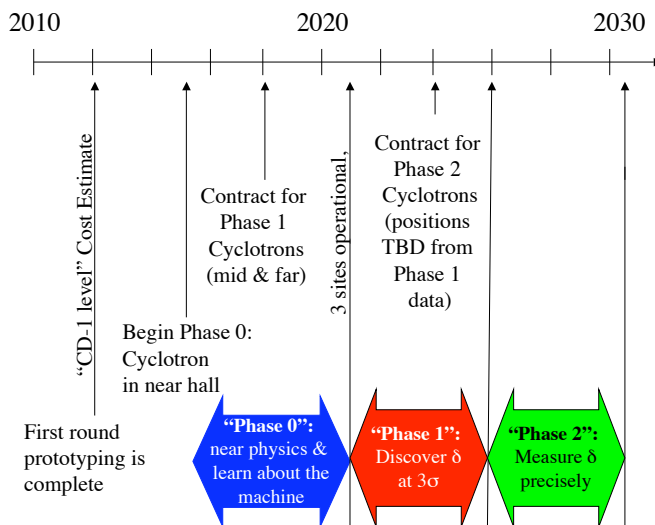


Figure 3.9: A possible plan for the staging DAE δ ALUS

at 10 MeV.

Current designs for the DUSEL water Cherenkov detector propose photocathode coverages between 30 and 40%. The latter is expected to provide sufficient performance for DAE δ ALUS while SK-II level coverage is likely insufficient for reconstructing the Gd capture gammas from IBD events. Choosing the middle ground, 30% coverage, though providing improved vertex and angular resolution, may also suffer from inefficient triggering of these signal events.

3.3 A Three-Phase Implementation Plan

We are developing our plans in coordination with the DUSEL Management. We propose a three-phase plan for staging the experiment, summarized in Fig. 3.9. Before the CP-violation studies begin, we propose a Phase 0 where we learn to run a single accelerator on-site. This would allow for near-accelerator physics to begin. At the same time, it allows us to understand



Figure 3.10: Sanford Lab footprint, showing the Kirk Adit and Oro Hondo sites.

important aspects of operation. Phase 1 and 2 represent the CP-violation studies periods.

For the Phase 0 site, we propose the area next to the entrance to the 300 L campus. This is called the Kirk Adit, and is labeled “Kirk Fans, 300 L Adit” on Fig. 3.10. This site is located just below the Yates shaft, at the base of a 300 ft rise, and 1.5 km from the detector. The two photographs in Fig. 3.11 show a portion of the space available. There is an open space available which is large enough for the accelerator (left photograph). However, it would be best if the unused fan building (right photograph) could be removed, as this allows more space. The entrance to the 300 L is obscured by the car in the left photograph. Sufficient power and water are available at the site. The entrance road would need improvements in the first 30 feet. However, the 300 L entrance may be used as a construction entrance, in which case the road improvements would be in place before the accelerator building would be built.

An alternative location for the on-site accelerator is at the Oro Hondo



Figure 3.11: Region in front of the Kirk Adit. Left: a portion of the open space available. The 300 L entrance is obscured by the car. To the right of the person is the fan building, not shown. Right: the building housing the unused fans.



Figure 3.12: The Oro Hondo substation site. Left: An area which could be cleared for the accelerator building; Right: view to the Yates shaft from the site.

substation (marked Oro Hondo on Fig. 3.10.) There is a flat area which could be easily cleared of small trees which would accommodate the accelerator building (Fig. 3.12, left). The area has power; water availability will need to be investigated. The road leading to the area is well maintained, because it leads to the Oro Hondo substation. The drawback of this site is that it is far from the Yates shaft (see Fig. 3.12, right, which shows the view to the Yates shaft). Thus it would not permit a 300 L physics program.

We do not proceed to CD-1 for Phase 1 until 2015 or later. This schedule allows time to negotiate the off-site locations. Several locations with disturbed land could be considered. By this timeframe, information will be available on $\sin^2 2\theta_{13}$ from Double Chooz, Daya Bay and T2K. These data can be used to inform our design.

Chapter 4

Impact On Other Analyses

In this section, we describe how DAE δ ALUS coordinates with other analyses already under consideration for the large water Cherenkov detector. We first show the benefits of the beam for calibration. We then discuss the impact of the beam events on other studies, especially those in particle-astrophysics, which are in the same energy range. It should be noted that there are DAE δ ALUS collaborators participating in each of these areas of study, and this allows good coordination between our design and those of the other analysis groups.

4.1 Neutrino-electron Events as a Calibration Source

Neutrino-electron events from the near accelerator offer a high statistics “standard candle” for calibration of the detector to the 1% level up to an energy of 55 MeV. This calibration standard will be valuable to all of the large detector experiments.

The neutrino-electron scattering process has a well-defined cross-section, as was discussed in Section 2.2, when we considered these events for the normalization sample. There is a net 1% theoretical error in the normalization of the cross section. However, there is negligible theoretical error in both the shape of the visible energy distribution and the scattering angle as a function of visible and neutrino energy. As a result, neutrino-electron scatters provide a very useful sample for calibration.

The visible energy distribution of neutrino-electron scatters from a decay

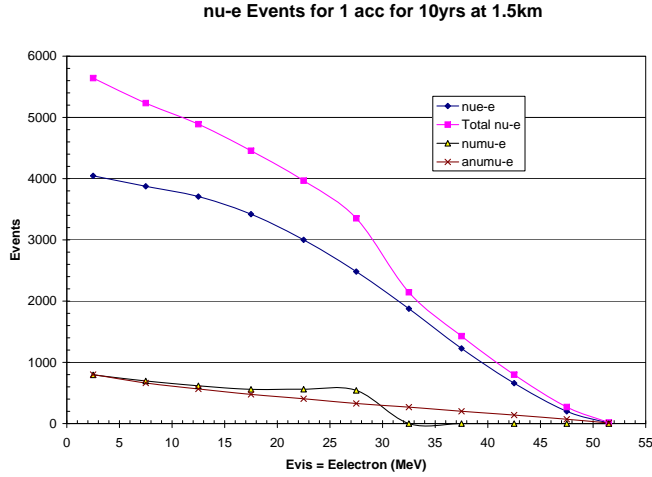


Figure 4.1: Top curve (magenta): visible energy distribution for neutrino-electron scatters from a decay-at-rest beam. Lower curves: the ν_e (blue), ν_μ (olive) and $\bar{\nu}_\mu$ (brown) contributions.

at rest beam is shown in Fig. 4.1, top curve (magenta). The number of events corresponds to 10 years of running at 1.5 km. The lower curves show the individual contributions of the three flavors in the beam: ν_e (blue), $\bar{\nu}_\mu$ (brown), and ν_μ (olive). Neutrino-electron scattering is dominated by the charged current ν_e -electron interaction. The scatters of the monoenergetic ν_μ (from π^+ decay) make an important contribution below 30 MeV. The $\bar{\nu}_\mu$ scatters are a small contribution.

Fig. 4.2 illustrates the strength of the neutrino-electron data for energy calibration. The plot shows the ratio of data with a 1% energy offset to the prediction, with the statistics for the full 10 year run. The poor χ^2/DOF indicates that calibration is required. This shows that this data set is sensitive at the $\sim 1\%$ level. Note that we allow the overall normalization to float since this data set is used to set the normalization of our analysis and that this calibration relies only upon shape.

There is a strong energy-angle dependence in the kinematics of neutrino-electron scattering. This is shown in Fig. 4.3 (right). As discussed in Sec-

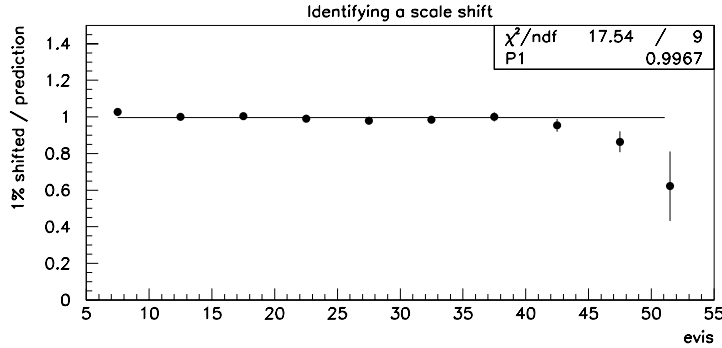


Figure 4.2: An example of an energy miscalibration in the detector. This plot shows the ratio of neutrino-electron events with a 1% energy miscalibration to the predicted shape. Note the poor χ^2/DOF and that the region near the endpoint is the most sensitive to miscalibrations.

tion 2.2, this allows the events from the near accelerator to be identified and separated from other sources of neutrino-electron scatters. A cut at $\cos\theta = 0.9$ with respect to the accelerator direction corresponds to an angular cut of 26° , which should account for angular resolution limitations. Fitting the events in this cone as a function of angle and visible energy will provide a measure of the angular resolution of the detector.

4.2 Impact On Other Large Detector Analyses

In this section we consider the impact of DAE δ ALUS events on the large detector analyses. We show that DAE δ ALUS has a negligible effect on all analyses except for the Supernova Relic Neutrinos (SRN) search. For the SRN analysis, we estimate that in the worst case our events degrade the 1σ limit for zero SRN events by 10% to 15%, while in the best case our events

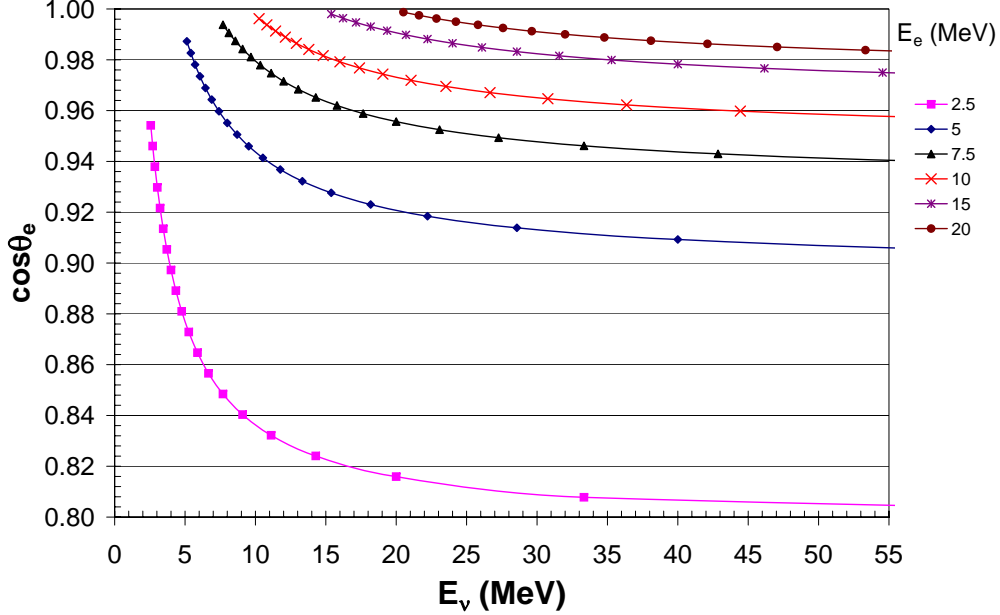


Figure 4.3: The unique angle vs. visible-energy correlation for neutrino-electron scattering at each neutrino energy.

provide a tool to improve the limit by 20% to 30%. We note that all of these analyses benefit from the neutrino-electron calibration sample provided by DAE δ ALUS.

4.2.0.1 High Energy Analyses: Long Baseline, Atmospheric and Proton Decay

The following analyses have signatures which require visible energy well above 55 MeV – the maximum for DAE δ ALUS – and/or event signatures which are easily distinguishable from DAE δ ALUS:

- Long Baseline Neutrino Oscillations, which employs a neutrino flux above 300 MeV.
- Atmospheric Neutrino Studies, which rely on ν_μ charged-current interactions above ~ 100 MeV.

- Proton Decay, where the signatures are $e^+\pi^0$ and $K^+\nu$. Both cases have a high visible energy and very different signature than DAE δ ALUS-induced interactions.

The proton decay analysis has overlapping interest with DAE δ ALUS because an important proton decay signature includes observation of a low energy photon. A 6 MeV photon accompanies proton decay in the oxygen nucleus, and thus provides a coincident signal that reduces background. This is of similar energy to the photons from the Gd-capture used by DAE δ ALUS. Both experiments will therefore require similar photocathode coverage.

4.2.0.2 Solar Analyses

DAE δ ALUS has a negligible effect on the solar neutrino analyses. The near accelerator produces a neutrino-electron scattering signal during the 20% time period that it is running. However, these events are cut by a $\cos\theta < 0.9$ requirement, where θ is the angle with respect to the near accelerator direction. This reduces the effective fiducial volume by 5%, but only when the accelerator is running. With only this cut, the net effect is a 1% loss of data. This can be cut to 0.5% if one simply requires that the accelerator run mainly when the sun is in the opposite hemisphere, which will place the accelerator events far outside of the angular cut for solar events.

On the other hand, the DAE δ ALUS events provide a very nice, well-defined, high statistics sample at low electron visible energies (see Fig. 4.1). Along with its value for calibration, already discussed, this sample allows a measurement of the efficiency for reconstructing neutrino-electron scatters at low energies. This may be valuable to the statistics-limited solar neutrino studies.

4.2.0.3 Supernova Burst Analyses

The Supernova Neutrino Burst Analysis focuses on the same energy range as DAE δ ALUS. A supernova neutrino signal will involve mostly IBD events (the contribution of ν -e scatters is a few percent, and from other interactions is not more than 10%). For an observed nearby supernova burst, which should involve at least 24,000 events in about 10 seconds in 300 kton for a supernova within 20 kpc (edge of the Galaxy), the expected background of Daedalus events is negligible. However, DAE δ ALUS events may be a background for extragalactic SN burst search analyses, which look for multiple events within

about a ten second time window, or look for single events in coincidence with external triggers such as optical supernovae or gravitational waves. In ten years of running there will be ~ 5000 fake bursts of two or more DAE δ ALUS events. By requiring IBD events for the supernova burst search, this background can be greatly reduced to the order of 1 in the 10-year period. For an ~ 2 hour time window in coincidence with a visible extragalactic supernova event, there will be on average about 3 Daedalus events, but the mean number of IBD events in such a window will be 0.04. This background can be reduced to zero by eliminating beam-on time from the supernova analysis, resulting in a some livetime loss.

4.2.0.4 Supernova Relic Neutrino Analyses

The one analysis for which the DAE δ ALUS events have a substantial overlap is the Supernova Relic Neutrino (SRN) search. We have been in contact with the leaders of the SRN analysis, in order to understand our impact [105, 106]. The conclusion of this interaction is that the two analysis groups can co-exist and, in fact, help one another.

Both analyses rely on IBD event signatures which will occur as single events (as opposed to bursts) spread over time. The SRN analysis focuses primarily on the 10 to 20 MeV range [106]. Above 20 MeV, invisible muons, which are below Cherenkov threshold, but stop and decay, dominate the SRN background. Below 10 MeV, natural background sources and reactor neutrinos dominate. The SRN 10 to 20 MeV window is adjacent to the DAE δ ALUS 20 to 55 MeV signal window. The DAE δ ALUS accelerators do produce a small number of events below 20 MeV.

To assess the impact of DAE δ ALUS events on this analysis, consider the case of no SRN signal. We consider the case of 5% and 10% systematic errors, to bracket a reasonable range for the analysis. We consider two energy bins, from 10 to 15 MeV, and from 15 to 20 MeV. We quote the factor by which the 1σ sensitivity of the SRN signal will change, for a $\delta_{CP} = 0$ and $\sin^2 2\theta_{13} = 0.04$ DAE δ ALUS signal. If the accelerators are not gated out, then the well-measured DAE δ ALUS signal can be subtracted, but that subtraction will have an error which impacts the SRN analysis. Rows 1 and 2 of Tab. 4.1 give the factor by which the sensitivity will change. An alternative is to gate out the 60% of the time that the three DAE δ ALUS accelerators are running. This weakens the SRN 1σ sensitivity by lowering the statistics

Energy bin	10-15 MeV	15-20 MeV
DAE δ ALUS, 5% SRN sys	1.14	1.24
DAE δ ALUS, 10% SRN sys	1.09	1.14
Gating out DAE δ ALUS, 5% SRN sys	1.12	1.19
Gating out DAE δ ALUS, 10% SRN sys	1.08	1.12
Likelihood, gating out DAE δ ALUS, 5% sys	0.5	0.59

Table 4.1: Factor by which the 1σ sensitivity will change for the SRN analysis, for various scenarios of including DAE δ ALUS, assuming a signal of $\delta_{CP} = 0$ and $\sin^2 2\theta_{13} = 0.04$. See text for explanation of scenarios.

for a potential SRN signal. The effect of this is shown in rows 3 and 4. In the energy range of the proposed analysis, in either case, the DAE δ ALUS impact is only a 10% to 20% worsening of the sensitivity.

On the other hand, the DAE δ ALUS events provide a substantial true IBD event sample in the 30 to 55 MeV range. This can be compared to the beam-off events in the 30 to 50 MeV range which are dominated by an order of magnitude by invisible muon events. These two samples can be played against one another to develop an algorithm which accepts true IBD events at high efficiency while rejecting invisible muon events. If one imagines developing a likelihood that rejects 50% of the invisible muon background while maintaining nearly 100% efficiency for IBD events, then the 1σ sensitivity for the SRN substantially improves. This is shown by row 5 of Tab. 4.1. Thus, depending on the quality of the likelihood which can be developed, the DAE δ ALUS events can provide a significant tool for improvement of the SRN analysis.

From this, one can see that the SRN and DAE δ ALUS analyses work well together. DAE δ ALUS provides extra motivation for Gd-doping and manpower for developing ideas like the likelihood analysis. In the other direction, DAE δ ALUS is relying on the development work on Gd-doping which was developed by the SRN community [3] and is now driven by the SRN and non-proliferation analysis groups.

Chapter 5

Conclusion

The DAE δ ALUS experiment offers an opportunity to both expand and enhance the neutrino physics program at DUSEL. Using a set of low-cost compact cyclotron sources, the experiment is able to provide a high-intensity, well-understood source of neutrinos for various studies from neutrino oscillations to nuclear spin structure measurements. Each stopped pion produced by incident protons leads to three different flavor neutrinos allowing the flux to be measured with little systematic uncertainty. In addition, the energy spectrum of the neutrinos is also completely determined by the weak decay of the stopped pion and stopped daughter muon. Thus, a stopped-pion neutrino beam provides an ideal laboratory for making precision normalized measurements in the region from 10 MeV to 55 MeV.

For neutrino oscillation measurements of θ_{13} or δ_{CP} , DAE δ ALUS would search for $\bar{\nu}_\mu \rightarrow \bar{\nu}_e$ oscillations where the $\bar{\nu}_e$ is detected through the inverse-beta-decay process where positron and neutron are detected and associated through a delayed coincidence. To enhance the neutron capture and detection, the detector will need to be doped with Gd. For the running scenario presented in this EOI with multiple MW-cyclotrons at distance of 1.5, 8, and 20 km from a 300 kton water detector, DAE δ ALUS has excellent discovery and measurement potential for θ_{13} and δ_{CP} that is comparable and complementary to the sensitivity of currently planned LBNE experiment. Also, since DAE δ ALUS can provide a high-statistics antineutrino sample, the combination of DAE δ ALUS with ν -only running of LBNE leads to an enhanced sensitivity (by a factor 2) for observing CP violation and measuring δ_{CP} .

A broad suite of non-oscillation physics experiments are also possible using the large LBNE detector or small dedicated detectors placed close to the

near (1.5 km) neutrino source. Coherent neutrino-nucleus scattering measurements using a 1 ton liquid argon detector placed 30 m from the source can be used to make measurements of the weak mixing angle or to search for non-standard interactions. A near source detector could also be used to measure cross sections relevant to astrophysical processes, supernova explosions and nucleosynthesis, and to supernova detectors. The high neutrino rates also lead to the possibility of searching for neutrino magnetic moments or making measurements of strange quark spin asymmetry, Δs .

The DAE δ ALUS experiment has two important requirements: the development of low-cost, high-power cyclotrons and the addition of Gd doping for the large LBNE detector. Significant R&D progress is being made in both of these areas and the prospects are good that attractive technical solutions will come about. If these requirements can be met, the DAE δ ALUS plus near source experiments will greatly enlarge the physics program at DUSEL. For these reasons, we request that the DAE δ ALUS experiment be incorporated as a possible option in the DUSEL planning with the understanding that the experiment would go forward when technical issues are addressed.

Bibliography

- [1] J. M. Conrad and M. H. Shaevitz. A New Method to Search for CP violation in the Neutrino Sector. 2009.
- [2] V. Barger et al. Report of the US long baseline neutrino experiment study. 2007.
- [3] John F. Beacom and Mark R. Vagins. GADZOOKS! Antineutrino spectroscopy with large water Cherenkov detectors. *Phys. Rev. Lett.*, 93:171101, 2004.
- [4] H. Watanabe et al. First Study of Neutron Tagging with a Water Cherenkov Detector. 2008.
- [5] S. Dazeley, A. Bernstein, N. S. Bowden, and R. Svoboda. Observation of Neutrons with a Gadolinium Doped Water Cerenkov Detector. *Nucl. Instrum. Meth.*, A607:616–619, 2009.
- [6] Atsuko Kibayashi and for the Super-Kamiokande Collaboration. Gadolinium Study for a Water Cherenkov Detector. 2009.
- [7] Gina Ramieka. Private Communication. 2009.
- [8] Joachim Kopp. Sensitivity Studies for LBNE.
- [9] Sanjib K. Agarwalla, Patrick Huber, Jonathan M. Link, and Debabrata Mohapatra. A new approach to anti-neutrino running in long baseline neutrino oscillation experiments. 2010.
- [10] A. Bandyopadhyay et al. Physics at a future Neutrino Factory and super-beam facility. *Rept. Prog. Phys.*, 72:106201, 2009.

- [11] Mauro Mezzetto. Next Challenge in Neutrino Physics: the $\theta(13)$ Angle. 2009.
- [12] The Neutrino Scientific Assessment Group. Recommendations to the Department of Energy and the National Science Foundation on a Future U.S. Program in Neutrino Oscillations. 2008.
- [13] The P5 Panel. Report of the Particle Physics Project Prioritization Panel,. 2008.
- [14] Hitoshi Murayama and T. Yanagida. Leptogenesis in supersymmetric standard model with right-handed neutrino. *Phys. Lett.*, B322:349–354, 1994.
- [15] Ernest Ma and Utpal Sarkar. Neutrino masses and leptogenesis with heavy Higgs triplets. *Phys. Rev. Lett.*, 80:5716–5719, 1998.
- [16] Sacha Davidson and Alejandro Ibarra. A lower bound on the right-handed neutrino mass from leptogenesis. *Phys. Lett.*, B535:25–32, 2002.
- [17] Junpei Harada. Neutrino mixing and CP violation from Dirac-Majorana bimaximal mixture and quark-lepton unification. *Europhys. Lett.*, 75:248–253, 2006.
- [18] Zhi-zhong Xing, He Zhang, and Shun Zhou. Nearly tri-bimaximal neutrino mixing and CP violation from mu - tau symmetry breaking. *Phys. Lett.*, B641:189–197, 2006.
- [19] Hiroshi Nunokawa, Stephen J. Parke, and Jose W. F. Valle. CP Violation and Neutrino Oscillations. *Prog. Part. Nucl. Phys.*, 60:338–402, 2008.
- [20] Thomas Schwetz, M. A. Tortola, and Jose W. F. Valle. Three-flavour neutrino oscillation update. *New J. Phys.*, 10:113011, 2008.
- [21] G. L. Fogli, E. Lisi, A. Marrone, A. Palazzo, and A. M. Rotunno. SNO, KamLAND and neutrino oscillations: $\theta(13)$. 2009.
- [22] Thomas Schwetz. Neutrino oscillations: Current status and prospects. *Acta Phys. Polon.*, B36:3203–3214, 2005.

- [23] Patrick Huber, Manfred Lindner, Thomas Schwetz, and Walter Winter. First hint for CP violation in neutrino oscillations from upcoming superbeam and reactor experiments. *JHEP*, 11:044, 2009.
- [24] Kendall Brianna McConnel Mahn and Michael H. Shaevitz. Comparisons and combinations of reactor and long-baseline neutrino oscillation measurements. *Int. J. Mod. Phys.*, A21:3825–3844, 2006.
- [25] Stefan Schonert. Neutrinoless double beta decay. *J. Phys. Conf. Ser.*, 203:012014, 2010.
- [26] D. S. Ayres et al. NOvA proposal to build a 30-kiloton off-axis detector to study neutrino oscillations in the Fermilab NuMI beamline. 2004.
- [27] Hisakazu Minakata. Long Baseline Neutrino Experiments with Two-Detector Setup. *Int. J. Mod. Phys.*, A23:3388–3394, 2008.
- [28] Patrick Huber, Joachim Kopp, Manfred Lindner, Mark Rolinec, and Walter Winter. New features in the simulation of neutrino oscillation experiments with GLOBES 3.0. *Comput. Phys. Commun.*, 177:432–438, 2007.
- [29] T. Araki et al. Measurement of neutrino oscillation with KamLAND: Evidence of spectral distortion. *Phys. Rev. Lett.*, 94:081801, 2005.
- [30] Y. Fukuda et al. Measurement of the flux and zenith-angle distribution of upward through-going muons by Super-Kamiokande. *Phys. Rev. Lett.*, 82:2644–2648, 1999.
- [31] I. Stancu et al. The OscSNS Whitepaper. D60, 2008.
- [32] R. L. Burman, M. E. Potter, and E. S. Smith. MONTE CARLO SIMULATION OF NEUTRINO PRODUCTION BY MEDIUM- ENERGY PROTONS IN A BEAM STOP. *Nucl. Instrum. Meth.*, A291:621–633, 1990.
- [33] R. L. Burman. Neutrino flux calculations for the ISIS spallation neutron facility. *Nucl. Instrum. Meth.*, A368:416–424, 1996.
- [34] P. Vogel and John F. Beacom. The angular distribution of the neutron inverse beta decay, $\text{anti-}\nu/e + p \rightarrow e^+ + n$. *Phys. Rev.*, D60:053003, 1999.

- [35] J. M. Conrad, J. M. Link, and M. H. Shaevitz. Precision measurement of $\sin^2(\theta_W)$ at a reactor. *Phys. Rev.*, D71:073013, 2005.
- [36] L. B. Auerbach et al. Measurement of electron-neutrino electron elastic scattering. *Phys. Rev.*, D63:112001, 2001.
- [37] W. C. Haxton. NEUTRINO REACTIONS ON OXYGEN AND A PROPOSED MEASUREMENT OF THE WEINBERG ANGLE. *Phys. Rev.*, C37:2660–2664, 1988.
- [38] R. Lazauskas and C. Volpe. Neutrino beams as a probe of the nuclear isospin and spin- isospin excitations. *Nucl. Phys.*, A792:219–228, 2007.
- [39] W. C. Haxton. The Nuclear Response of Water Cherenkov Detectors to Supernova and Solar Neutrinos. *Phys. Rev.*, D36:2283, 1987.
- [40] Weller H.R. Tilley, D.R. and C.M. Cheves. Energy levels of light nuclei, $A = 16$ (see Tab. 16.30). *Nucl. Phys.*, A564, 1993.
- [41] F. Ajzenberg-Selove and T. Lauritsen. Energy levels of light nuclei, $A = 17$ (see tab. 17.6). *Nucl. Phys.*, 11, 1959, Revised Nov., 2008.
- [42] F. Ajzenberg-Selove and T. Lauritsen. Energy levels of light nuclei, $A = 18$ (see Tab. 18.4). *Nucl. Phys.*, A475, 1959, Revised Nov., 2008.
- [43] Perry R.T Charlton W.S Wilson, W.B. and T.A. Parish. Sources: A code for calculating (α , n), spontaneous fission, and delayed neutron sources and spectra. *Prog. in Nuc. Energy*, 51:608, 2009.
- [44] Y. Ashie et al. A Measurement of Atmospheric Neutrino Oscillation Parameters by Super-Kamiokande I. *Phys. Rev.*, D71:112005, 2005.
- [45] T. Adams et al. Terascale Physics Opportunities at a High Statistics, High Energy Neutrino Scattering Experiment: NuSONG. *Int. J. Mod. Phys.*, A24:671–717, 2009.
- [46] F. James and M. Roos. Minuit: A System for Function Minimization and Analysis of the Parameter Errors and Correlations. *Comput. Phys. Commun.*, 10:343–367, 1975.
- [47] Mary Bishai. Private Communication. 2009.

- [48] Charles J. Horowitz, K. J. Coakley, and D. N. McKinsey. Supernova observation via neutrino nucleus elastic scattering in the CLEAN detector. *Phys. Rev.*, D68:023005, 2003.
- [49] K. Scholberg et al. The CLEAR Experiment. 2009.
- [50] Kate Scholberg. Prospects for measuring coherent neutrino nucleus elastic scattering at a stopped-pion neutrino source. *Phys. Rev.*, D73:033005, 2006.
- [51] G. P. Zeller et al. A precise determination of electroweak parameters in neutrino nucleon scattering. *Phys. Rev. Lett.*, 88:091802, 2002.
- [52] Vernon D. Barger, G. F. Giudice, and Tao Han. Some New Aspects of Supersymmetry R-Parity Violating Interactions. *Phys. Rev.*, D40:2987, 1989.
- [53] S. Davidson, C. Pena-Garay, N. Rius, and A. Santamaria. Present and future bounds on non-standard neutrino interactions. *JHEP*, 03:011, 2003.
- [54] J. Schechter and J. W. F. Valle. Neutrino Masses in $SU(2) \times U(1)$ Theories. *Phys. Rev.*, D22:2227, 1980.
- [55] P. S. Amanik and G. C. McLaughlin. Nuclear neutron form factor from neutrino nucleus coherent elastic scattering. *J. Phys.*, G36:015105, 2009.
- [56] K. Langanke et al. Electron capture rates on nuclei and implications for stellar core collapse. *Phys. Rev. Lett.*, 90:241102, 2003.
- [57] W. R. Hix et al. The consequences of nuclear electron capture in core collapse supernovae. *Phys. Rev. Lett.*, 91:201102, 2003.
- [58] A. Juodagalvis, K. Langanke, W. R. Hix, G. Martinez-Pinedo, and J. M. Sampaio. Improved estimate of stellar electron capture rates on nuclei. 2009.
- [59] Nu-SNS Proposal.

- [60] G. C. McLaughlin. Neutrino nucleus cross section measurements using stopped pions and low energy beta beams. *Phys. Rev.*, C70:045804, 2004.
- [61] C. Frohlich et al. Neutrino-induced nucleosynthesis of $A \lesssim 64$ nuclei: The ν p- process. *Phys. Rev. Lett.*, 96:142502, 2006.
- [62] L. T. Kizivat, G. Martinez-Pinedo, K. Langanke, R. Surman, and G. C. McLaughlin. Gamma-Ray Bursts Black hole accretion disks as a site for the ν p-process. *Phys. Rev.*, C81:025802, 2010.
- [63] Gail C. McLaughlin and George M. Fuller. Evidence for an intense neutrino flux during r process nucleosynthesis? *Astrophys. J.*, 464:L143–L146, 1996.
- [64] Y. Z. Qian, W. C. Haxton, K. Langanke, and P. Vogel. Neutrino-induced neutron spallation and supernova r- process nucleosynthesis. *Phys. Rev.*, C55:1532–1544, 1997.
- [65] P. Vogel and J. Engel. Neutrino Electromagnetic Form-Factors. *Phys. Rev.*, D39:3378, 1989.
- [66] G. Garvey, E. Kolbe, K. Langanke, and S. Krewald. Role of strange quarks in quasielastic neutrino scattering. *Phys. Rev.*, C48:1919–1925, 1993.
- [67] R. Tayloe. A measurement of the strange quark contribution to the nucleon spin via neutrino nucleon elastic scattering. *Nucl. Phys. Proc. Suppl.*, 105:62–65, 2002.
- [68] M. B. Barbaro, A. De Pace, T. W. Donnelly, A. Molinari, and M. J. Musolf. Probing nucleon strangeness with neutrinos: Nuclear model dependences. *Phys. Rev.*, C54:1954–1969, 1996.
- [69] F. T. Avignone, V. Gudkov, L. Chatterjee, Yu. Efremenko, and M. Strayer. ORLaND: A proposed facility to investigate neutrino properties relevant to astrophysics. *Nucl. Phys. Proc. Suppl.*, 91:113–119, 2001.
- [70] Timothy Antaya. Talk Given at the DAE δ ALUS Workshop, Feb. 2010.

- [71] Robert Macek. Private Communication. 2009.
- [72] Th. Stammbach et al. The feasibility of high power cyclotrons. *Nucl. Instr. & Meth.*, B11, 1-4:1–7, 1996.
- [73] H.G. Blosser and D.A. Johnson.
- [74] H.G. Blosser et al. Advances in superconducting cyclotrons at nscl. *Cyclotrons and Their Applications, Eleventh International Conference*, pages 157–167, 1986.
- [75] S. Zarembo W. Beeckman D. Vandeplassche M. abs P. Verbruggen W. Kleeven, S. Lucas and Y. Jongen. The self-extracting cyclotron. *Cyclotrons and Their Applications, Sixteenth International Conference*, AIP 0-7354-0044-X:69–73, 2001.
- [76] W. Kleeven Y. Jongen and S. Zarembo. New cyclotron developments at iba. *Cyclotrons and Their Applications, Seventeenth International Conference*, pages 69–73, 2004.
- [77] A.K. Ghosh et al. Dynamic stability threshold in high-performance internal-tin nb₃sn superconductors for high field magnets. *Supercond. Sci. Technol.*, 18:L5–L8, 2005.
- [78] <http://abe.web.psi.ch/accelerators/ringcyc.php>.
- [79] L. Calabretta et al. A Superconducting Ring Cyclotron To Deliver High Intensity Proton Beams. *Proceedings of EPAC 2000*, page 917, 2000.
- [80] Kawaguchi et al. Design of the sector magnets for the riken superconducting ring cyclotron, us particle accelerator conference, 1997. *IEEE*, 1998.
- [81] The T2K Experiment. <http://jnusrv01.kek.jp/public/t2k/index.html>.
- [82] Experiments at the JPARC Hadron Hall. http://j-parc.jp/nuclpart/slowextracted_e.html.
- [83] Minos Experiment and the NuMI Beamline. <http://www-numi.fnal.gov/>.

- [84] LANSCE Facility Status. <http://lansceoperations.lanl.gov/>.
- [85] ISIS: A World Center for Neutrons and Muons. <http://www.isis.stfc.ac.uk/index.html>.
- [86] R. L. Burman and W. C. Louis. Neutrino physics at meson factories and spallation neutron sources. *J. Phys.*, G29:2499–2512, 2003.
- [87] R. L. Burman and P. Plischke. Neutrino fluxes from a high-intensity spallation neutron facility. *Nucl. Instrum. Meth.*, A398:147–156, 1997.
- [88] J. F. Crawford et al. Measurement Of Cross-sections And Asymmetry Parameters For The Production Of Ccharged Pions From Varius Nuclei By 585- MeV Protons. *Phys. Rev.*, C22:1184–1196, 1980.
- [89] D. R. F. Cochran et al. Production of charged pions by 730-MeV protons from hydrogen and selected nuclei. *Phys. Rev.*, D6:3085–3116, 1972.
- [90] P. Denes et al. Production Of Positive Pions By 800-MeV Protons On Carbon. *Phys. Rev.*, C27:1339–1341, 1983.
- [91] N. J. Digiacomio et al. Inclusive Pion Production In 330-MeV, 400-MeV, And 500-MeV Proton Nucleus Collisions. *Phys. Rev.*, C31:292–294, 1985.
- [92] R. C. Allen et al. A Measuement Of The Neutrino Flux From A Stopped Pion Source. *Nucl. Instrum. Meth.*, A284:347, 1989.
- [93] A. Wehmann. Fnal document numi-b-493. 1999.
- [94] A.A. Abramov. Fnal document numi-b-652. 2000.
- [95] J.Hylen. Fnal document numi-b-652. 2000.
- [96] M. Apollonio et al. Limits on neutrino oscillations from the chooz experiment. *Phys. Lett. B*, pages 415–430, 1999.
- [97] N. S. Bowden, A. Bernstein, M. Allen, J. S. Brennan, M. Cunningham, J. K. Estrada, C. M. R. Greaves, C. Hagmann, J. Lund, W. Mengesha, T. D. Weinbeck, and C. D. Winant. Experimental results from an antineutrino detector for cooperative monitoring of nuclear reactors. *NIM A*, 572:985–998, 2007.

- [98] S. Dazeley, A. Bernstein, N.S. Bowden, and R. Svoboda. Observation of neutrons with a gadolinium doped water cherenkov detector. *NIM A*, 607:616–61, 2009.
- [99] Hirokazu Ishino for the Super-Kamiokande Collaboration. Gadolinium study for super-kamiokande, 2009.
- [100] R. W. Kadel. Dusel long base line neutrino experiment (lbne) water supply and requirements, v2. Technical report, LBL, 2010. DDRD-doc-392-v2.
- [101] Mark Vagins. Gadzooks Supernova neutrinos without the annoying wait, 2010. <http://theory.tifr.res.in/jigsaw10/talks/vagins.pdf>.
- [102] W. Coleman, A. Bernstein, S. Dazeley, and R. Svoboda. Transparency of 0.2% gdcl3 doped water in a stainless steel test environment. *NIM A*, 595:339–345, 2008.
- [103] J. Hosaka et al. Solar neutrino measurements in Super-Kamiokande-I. *Phys. Rev.*, D73:112001, 2006.
- [104] J. P. Cravens et al. Solar neutrino measurements in Super-Kamiokande-II. *Phys. Rev.*, D78:032002, 2008.
- [105] John Beacom. Private Communications. 2009, 2010.
- [106] Mark Vagins. Private Communication. 2010.